Additive Manufacturing 61 (2023) 103348

Contents lists available at ScienceDirect

Additive Manufacturing

journal homepage: www.elsevier.com/locate/addma

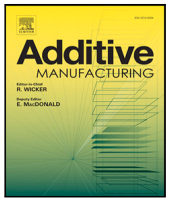

Research paper

Mechanical analysis and optimized performance of G-Code driven material extrusion components

Iván Rivet [a,*], Narges Dialami [a], Miguel Cervera [a], Michele Chiumenti [a], Quino Valverde [b]

[a] International Center for Numerical Methods in Engineering (CIMNE), Universidad Politécnica de Cataluña, Campus Norte UPC, 08034, Barcelona, Spain
[b] Departamento de Ingeniería, Sección Ingeniería Mecánica, Pontificia Universidad Católica del Perú, Lima, Peru

ARTICLE INFO

Keywords:
Additive manufacturing
Optimization
G-code
Mechanical performance
Voxelization

ABSTRACT

In this work an end-to-end optimization procedure to maximize the mechanical performance of Additive Manufacturing (AM) components is presented. Material Extrusion (ME) is the selected demonstrative AM technology, but the approach is applicable to other AM processes where the manufacturing toolpaths of the geometry of the printed component are described in G-Code format. The proposed methodology is integrated into the AM workflow and drives a two-step optimization process in order to select the optimal printing orientation for a user defined case. The G-Code file containing the manufacturing toolpaths is used as input. This approach allows to operate as close as possible to the geometry of the actual component, avoiding the use of the STereoLithography (STL) geometry. A voxelized mesh is built from the G-Code by solving a modified 2.5D Shortest Path Problem (SPP) and high-fidelity Finite Element (FE) simulations are performed with the resulting mesh. A printing pattern-based material model that distinguishes three different zones of the printed component is used. Due to the orthotropic nature of the ME process, the Tsai–Wu failure criterion is applied to obtain the indicators of the mechanical performance of the component. These computed metrics are used to drive an optimization process where a robust criterion based on the Machine Learning (ML) algorithm Anomaly Detection (AD) is applied in order to select the optimal build direction from a prespecified span of orientations. Two test cases and one case study illustrate the performance of the proposed methodology. The results validate the approach against experiments, indicate that the selected optimization criterion is robust against factors alien to the actual physical problem and show that the accuracy of the voxelized method greatly improves the "traditional" STL-based simulations.

1. Introduction

Additive Manufacturing (AM) has enabled the creation of intricate parts that used to be expensive and difficult to fabricate [1,2]. Among all the AM techniques that have been developed [3], Material Extrusion (ME) has become predominant due to its ease of use and its reduced cost compared to the others [4].

In ME the printing head melts the filament into a semi-liquid state [5,6], extrudes molten materials, and deposits single layers onto the build platform [7,8]. ME has become a suitable and viable option for small production lots of thermoplastic parts as it eliminates the cost of mold making. Very recently this paradigm has evolved from rapid prototyping to full-scale production concerning a more flexible [9] and efficient fabrication [10,11]. This flexibility requires a wide knowledge of a process with great complexity such as ME [12].

The different stages in the ME process, and also in several AM technologies, are linked by the so-called G-Code format defined by the ISO 6983 [13]. The G-Code consists of plain text where each line represents a different command involving the manufacturing toolpaths that the device must reproduce as well as other process specifications such as speed, material feeding or tools information [14]. In ME the G-Code is generated from a CAD file by slicing programs, such as Simplify [15] or Slic3r [16], where the component is intersected by horizontal planes separated at a specified height. The result of each intersection is converted into a manufacturing path and is called layer. Each layer is then sequentially built in ascending order.

This manufacturing strategy makes the build orientation to influence several aspects of the printed component, such as the surface quality [17], the amount of support material, the build time or the fabrication cost [6]. However, the build orientation has a greater impact on the structural properties of ME parts, and so mechanical analysis and performance are the scope of the present paper. The material properties

* Corresponding author.
E-mail addresses: irivet@cimne.upc.edu (I. Rivet), narges.dialami@upc.edu (N. Dialami), miguel.cervera@upc.edu (M. Cervera), michele.chiumenti@upc.edu (M. Chiumenti), qvalver@pucp.edu.pe (Q. Valverde).

https://doi.org/10.1016/j.addma.2022.103348
Received 18 July 2022; Received in revised form 25 November 2022; Accepted 3 December 2022
Available online 19 December 2022

of the final ME component differ from the (isotropic) raw material, resulting in a behavior with a remarkable degree of anisotropy [18]. Therefore, a clear understanding of the build orientation-properties dependency becomes crucial in order to optimize the performance of ME parts.

In addition to build orientation, printing parameters such as layer thickness, printing pattern or infill density also influence the final mechanical properties, but their impact is lower [19]. For instance, infill density also allows to reduce the printing time and the material consumption to the detriment of the mechanical performance of the component, but maintaining its specific mechanical properties [20]. Therefore it is pointless to consider it when optimizing only the part mechanical performance.

Two main methodologies can be distinguished in the field of the build orientation optimization, namely one-step and two-step methods [21]. One-step methods compute the results for a given orientation and, if a certain criterion is satisfied (meaning the solution space has been traversed), the search terminates; if not, the model is rotated for a specific step size and the process is repeated. In contrast, two-step methods calculate in advance the set of all possible optimal orientations; then the best one is selected based on the imposed criteria.

Several researches based on the one-step method have been developed to study the influence of ME process parameters in the mechanical performance, build quality or dimensional accuracy of the final part and its optimization [22–24]. Multiple studies [25–27] proceed with regressions on experimental models and then perform a search approach via methodologies such as genetic algorithms, principal component analysis or particle swarm optimization. In [28] a relationship between the mechanical properties of the component and its printing orientation is established via tensile test experiments. The authors in [29] optimized the mechanical performance of SLA/ME parts based on a model that took into account the number of the part critical sections, their height, the maximum normal stress at that location and the angle between the section and the part orientation. These studies do not take into account the multiple printing patterns present in a component and they are applicable only for simple structures. Other researches [30,31] make use of statistical designs (mainly ANOVA) to establish the impact of certain process parameters on the final part properties, but either the optimal parameters are not determined or the results are not applicable to more complex cases. From the literature review, it follows that if the optimization process is driven by estimation models the methodology is case-dependent.

Numerous works in recent years follow the two-step methodology for optimizing various properties of ME components [32,33]. The authors in [34,35] presented a method for determining the optimal build orientation that optimizes the surface roughness, build time and part cost of AM parts based on user-specified weights. In [36] the authors classified the different geometrical features in a STL file into cylinders, planes and cones. Then different orientation candidates were assigned to each feature, and all non-duplicated orientations were analyzed. Ulu et al. [37] maximized the factor of safety of ME components under prescribed loading and boundary conditions by modifying the build orientation of the component. They developed a selection algorithm with a surrogate model that minimized the number of orientations to analyze via computational simulations. Nevertheless, they were using conservative estimates when analyzing the mechanical performance of the configuration and no suitable failure criterion was applied. In addition, the optimization in all these researches was performed on the STL file rather than on the generated G-Code file, and no distinction between the printing patterns is made.

Among all these studies only a few optimize the properties of 3D printed parts and automatize the process with the focus on its extrapolation to different use cases [37,38]. In [39] the part topology, support and build orientation are optimized in order to improve the printability of components. In [40] a material redistribution inside the part is performed, as well as the modification of the nozzle diameter and the layer height, for improving the mechanical properties of ABS parts. Nguyen et al. [41] studied an optimization of the build orientation and the concurrent density distribution of the lattice structures for maximizing the component performance. Liu et al. [42,43] developed a method in which deposition path and topology optimization strategies are concurrently applied to optimize the structural performance of AM parts. The anisotropic nature of ME components is taken into account, and the structural performance is enhanced by matching the deposition path with the principal stress direction. However, all these researches focus on a generalized optimization of certain process parameters without going in depth in its actual implementation [44,45] and are far from proposing an end-to-end solution integrated with the actual AM workflow.

In this work, a two-step optimization algorithm for AM parts that selects the build orientation with the best mechanical performance is developed. This novel approach includes from the G-Code generation to the manufacturing of the final component. The manufacturing information present in the G-Code file plays a significant role in predicting the performance of the final component; using it to conduct the optimization process is beneficial, as it significantly increases the accuracy of the simulations. Finite Element (FE) simulations are performed on each orientation in order to characterize its structural robustness. By using this strategy, the user can model static simulations, select process parameters and perform numerical calculations to produce stress/strain metrics during part operation. These results are used to drive an optimization problem that computes the optimal build direction against user-defined goals.

Typically, complex geometries require a great number of scanning toolpaths to define the G-Code, which translates into a very fine mesh with high computational cost [46]. The proposed strategy uses an adaptive mesh strategy with an octree based coarsening [47], allowing for the coarsening of the mesh in the geometrically uncomplicated regions of the component and significantly reducing the computational cost.

A material model based on the printing pattern is used in this paper. This model has been developed and validated in the previous works of the authors [48–50]. In this modelization each printing pattern of the component represents a material with its corresponding properties: outer shells, defined by aligned filaments; top/bottom shells, formed by crossed filaments; and inner, where multiple user-defined patterns can be selected.

The main contributions of this work are:

(1) An end-to-end optimization algorithm integrated in the AM workflow where the material is modeled by making a distinction between different printing patterns.
(2) A novel statistical criterion that determines the optimal build orientation, where its structural robustness is calculated based on an orthotropic failure criterion.
(3) A FE domain generated from a G-Code and the use of an adaptive octree-based mesh strategy.

The paper is organized as follows. First, Section 2 introduces the proposed end-to-end methodology. Sections 2.1 and 2.2 present the developed strategy for the generation of the FE mesh from the G-Code. Section 2.3 explains the definition of the boundary conditions (BCs) in the generated FE mesh. The applied material model is described in Section 2.4 and the optimization loop is developed in detail in Section 2.5. The methodology is demonstrated on two test cases in Section 3 and its industrial application is shown on a case study in Section 4. Finally, Section 5 presents some conclusions and lines for future development.

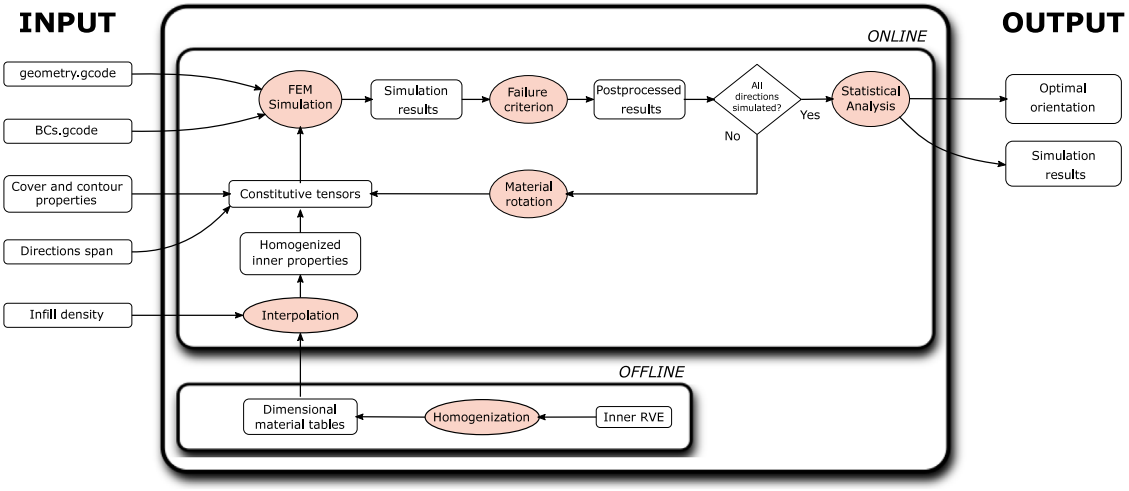

Fig. 1. Optimization methodology scheme.

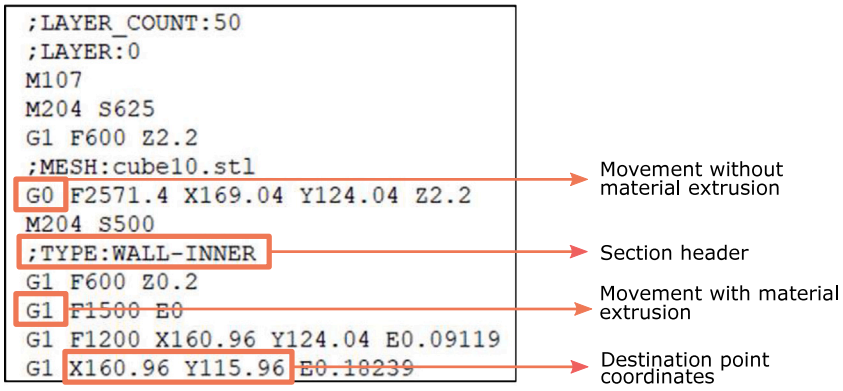

Fig. 2. G-Code file sample.

2. Methodology

In this section the methodology followed to optimize the build orientation of the component is explained. The G-Code files, the material properties, the printing orientations to simulate and the selected infill density are used as input for the tool.

The inner zone is heterogeneous and is formed by a repetitive cell structure. This cell is identified as the Representative Volume Element (RVE). A computational homogenization technique is applied to the RVE in order to represent the behavior of the inner zone as a homogeneous continuum and save computational resources [51]. The properties of the homogenized RVE are computed offline and do not depend on the material of the component. Thus, the infill material properties are interpolated from offline precomputed tables with the actual infill density value [49].

These properties, alongside the shell properties, are used for building the component constitutive tensors. Then the FE simulation is performed and the chosen failure criterion is applied to the results. This process is repeated for all the specified directions, which are defined as three consecutive rotations around the X, Y and Z axis of the original orientation. However, the procedure is applicable to any arbitrary building orientation. Finally, a statistical analysis is applied to the overall results in order to decide the optimal build orientation. The whole process scheme is shown in Fig. 1.

Hereafter the G-Code file with the manufacturing toolpaths that define the geometry will be called geometry.gcode, while the file containing the Boundary Conditions (BCs) information, which includes the imposed loads, displacements and clampings as well as their location, will be referred to as BCs.gcode.

2.1. Meshing strategy from G-code files

The generation of the mesh for the FE simulations is explained in this section. The ME roadmap starts with the slicing process of the component to be manufactured. Once the geometry has been prepared and the user has defined the different print settings layer thickness, extrusion temperature, axis speed and infill pattern among others, the resulting STereoLithography (STL) mesh is sliced at specific heights and the G-Code is generated for later uploading to the 3D printer. This process is made internally by the slicer and involves several complexities. Although all slicers follow similar strategies, their algorithms may slightly differ from one to other. However, this difference may be noticeable only for complex models. Among all the open-source slicers Cura is the most popular option and the one used in this paper [52].

G-Code is a low-level language and is defined by numerical codes such as G, M, T or F. It expresses not only coordinates for the movements but also defines printing parameters such as extrusion temperature or feed rate. However, for the mesh generation only two fields, highlighted in Fig. 2, are required: the coordinates, mainly indicated by the instructions G0, when a movement is made without material extrusion, and G1, when material is extruded; and the current material zone, which defines the printing pattern and its corresponding material properties, as it will be shown in Section 2.4.

The use of a G-Code file as input for mesh generation is convenient for two reasons: (i) to avoid reading the STL geometry and a possible repairing process, and (ii) to operate as close as possible to the actual part due to the fact that the same information is used for the manufacturing.

In order to substitute the STL model in the analysis, a voxelized geometry is generated instead. Voxelization is a volume representation

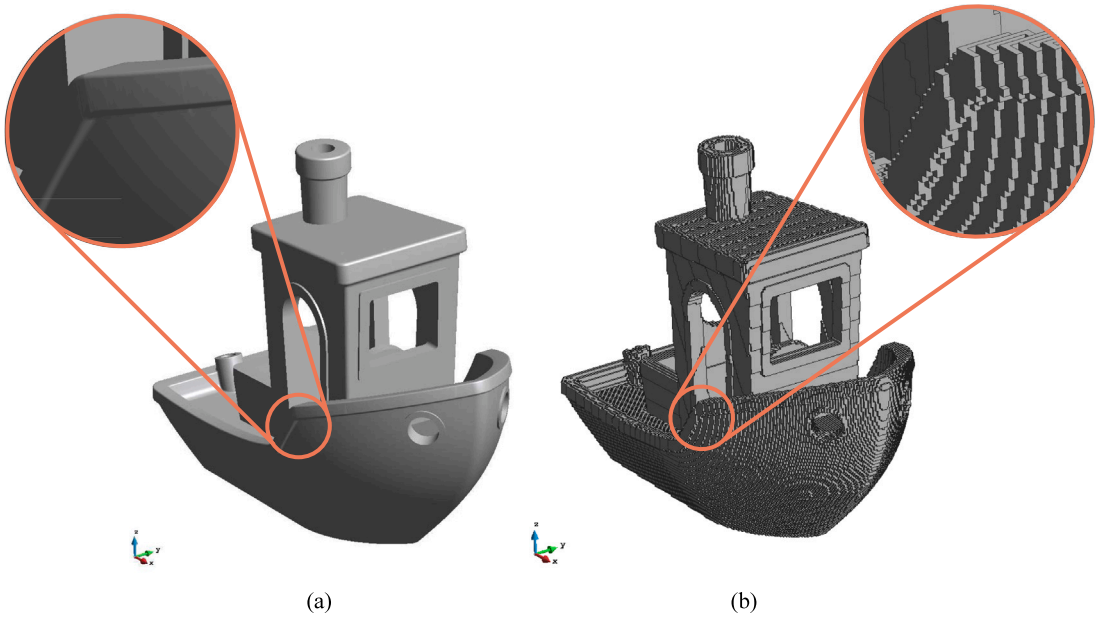

Fig. 3. 3DBenchy Voxelization example. (a) STL geometry. (b) Voxelized geometry.

scheme for CAD models that encodes the information of the solid geometry in a structured 3D rectangular grid containing volume elements called "voxels" [53]. The main benefit of the voxelization is that it allows to roll-back from the G-Code to the actual model by using efficient Boolean operations based on collision detection algorithms. With this approach the volumetric data associated with the CAD model is preserved, meaning that the mesh fidelity is better than when constructing the mesh directly from the STL file, which is an aspect of particular importance for AM [54]. In addition, in the voxelized mesh all the elements are hexahedrons with an aspect ratio close or equal to 1, showing a higher mesh quality than one generated from an STL file.

The geometry.gcode file is used as an input for the voxelization procedure to obtain a cartesian mesh as shown in Fig. 3. In this process, the printing space is constrained to a bounding box defined by the maximum and minimum coordinates on each direction of the G-Code, and later subdivided into voxels, where each one of them is activated if and only if a G1 instruction intersects it. The size of the voxels in the X, Y and Z directions is defined by the meshing strategy explained in Section 2.2

Since the AM process is a layer by layer procedure, the voxelization is reduced to a 2.5D mathematical problem. Consequently, the intersection of the voxels on each layer is treated as a rectangle-2D segment intersection in order to save computational resources. However, computing a one-vs-all algorithm where each path is checked against every single voxel is computationally inefficient. Instead, a modified Shortest Path Problem (SPP) is used [55]. In this SPP the shortest path between two squares in a uniform grid is calculated. As depicted in Fig. 4, not only the starting (x_0, y_0) and ending voxel (x_f, y_f) indices must be taken into account, but also the position of the starting (h_0, v_0) and ending (h_f, v_f) path points in their respective voxels. The followed walk-grid algorithm used to solve the SPP is summarized in Algorithm 1.

2.2. Octree mesh coarsening

A small element size is required to correctly intersect the toolpath and avoid losing information of the geometry. However, it is inefficient to maintain a fine mesh in the whole domain since this may imply very expensive simulations. Additionally, the infill zone has been homogenized in order to avoid its high-fidelity discretization. To overcome this issue an adaptive meshing strategy is applied [47,56], where a variable

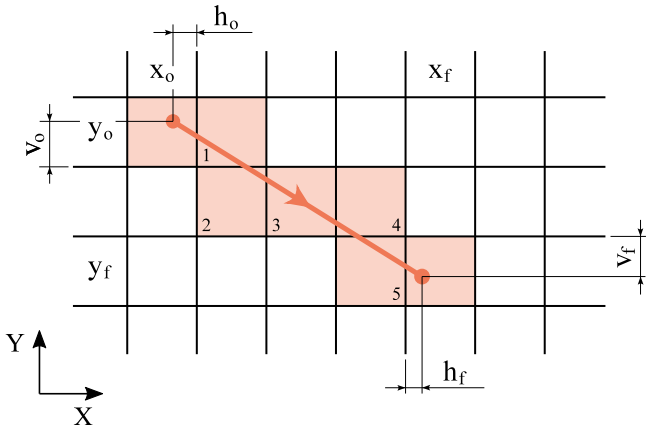

Fig. 4. Shortest path of voxels on a rectangular grid.

Algorithm 1: Walk-Grid Algorithm

Data: The binary matrix $\mathbf{B} \in \mathbb{R}^{N \times M}$ representing the current layer of voxels, (h_0, v_0), (h_f, v_f), (x_0, y_0) and (x_f, y_f)
Result: the updated binary matrix **B**

$i \leftarrow x_0$; $j \leftarrow y_0$;
while $i \neq x_f$ *or* $j \neq y_f$ **do**
  $h_p \leftarrow \frac{h_0+(i-x_0)}{x_f-x_0}$; /* Percentage of traversed horizontal path */
  $v_p \leftarrow \frac{v_0+(j-y_0)}{y_f-y_0}$; /* Percentage of traversed vertical path */
  if $h_p \leq v_p$ **then**
    $i \leftarrow i+1$; /* Advance in the X direction */
  else
    $j \leftarrow j+1$; /* Advance in the Y direction */
  $B_{ij} = 1$; /* 1 indicates an intersected voxel and 0 an empty volume */

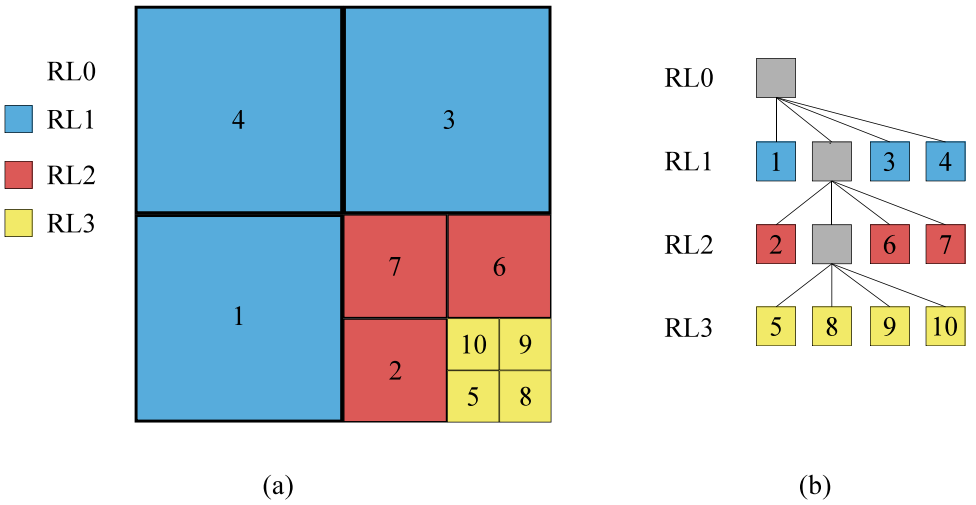

Fig. 5. Octree scheme in a 2D view. (a) Octree mesh representation. (b) Octree with labeled elements, where numbers and no numbers indicate child and parent elements respectively.

element size is used allowing for a coarser mesh in some areas of the component as shown in Fig. 6.

This methodology starts with a single (parent) element of size equal to the bounding box. The element is successively divided in 8 equal-sized (children) elements until reaching the desired resolution. Every time that the voxel is divided a new Refinement Level (RL) is created, and the maximum number of RLs is pre-specified by the user.

The different RLs define an octree hierarchy system. The initial bounding box is set to the RL 0, being this voxel the parent of the level 1 voxels. In the same way, level 1 voxels are the children from level 0 and the parents of level 2 voxels, etc. An octree scheme showing the parent–child relationship is shown in Fig. 5

The strategy can be summarized as follows. At each G-Code instruction a series of adaptivity cycles are performed. On each cycle, every voxel is successively refined if it contains the analyzed hatch, until reaching the maximum RL (Fig. 6(c)). All the newly intersected voxels are added to the component domain, and a coarsening is performed in the already intersected voxels (Fig. 6(d)) based on the selected criterion. Next, the following G-Code instruction is read and the process is repeated until the end of the G-Code file.

Multiple criteria can be applied for deciding whether a coarsening is performed or not. In this work a geometrical criterion is selected. At each G-Code instruction, all elements that already have been intersected are set to be coarsened. When all the children elements from the same parent element satisfy this condition, they are merged into one (parent) element.

This process must take into account the different printing patterns present in the component. Therefore the children elements are coarsened only when all of them belong to the same printing pattern.

2.3. Boundary conditions

In this section the definition of the BCs on the generated FE domain is explained. The FE mechanical simulation requires a set of load and displacement conditions to be specified. Since the initial CAD geometry, where the user has defined these specifications, has been transformed into a layered toolpath, these conditions must also be transformed to the G-Code format (Fig. 7(b)). A python script is used to intersect the user-selected surfaces, where the BCs are applied, with horizontal planes and to translate them into a G-Code. The generated BCs.gcode is later intersected with the voxels (Fig. 7(a)) to form the annotated mesh (Fig. 7(c)). These annotated voxels can present either prescribed displacements (Dirichlet BCs) or applied loads (Neumann BCs). For the former ones, the prescribed values are passed to the voxel nodes, while for the latter ones, the surface load is transformed into an equivalent volume load applied to the voxels intersected.

Table 1
Printing pattern corresponding to each CURA section.

Section	Printing pattern
WALL-INNER	Aligned
WALL-OUTER	Aligned
SKIN	Crossed
FILL	Infill
Auxiliary structures	(Not present)

2.4. Orthotropic material model and failure criterion

In this section the used material model that distincts the different printing patterns of an AM component is explained. A printed part can be divided into three different zones based on their printing pattern: top and bottom shells, outer shell and inner. Two different types of inner zones exist: infill and lattice structures. Top and bottom shells are printed using crossed filaments, outer shells with aligned filaments and inner may present different printing patterns, with the ±45°orientation being the most prevalent. Each one of these zones behaves as an orthotropic material and is treated as such. In previous works of the authors, a material model that distinguishes these zones has been tested and validated [48,49]. Crossed and aligned filaments are characterized using tensile tests, while for the inner computational homogenization of its RVE is used. Most recently the crossed and aligned filaments have also been successfully characterized via computational homogenization by identifying their respective RVE [50]. The use of a homogenization strategy allows to analyze complex topologies such as lattice or organic structures.

Unlike STL files, G-Code already distincts the different printing patterns of an AM component, which is very advantageous when assigning the materials to the generated FE mesh.

A total of 5 different sections are labeled in a G-Code: WALL-INNER, WALL-OUTER, SKIN, FILL and auxiliary structures (SKIRT, SUPPORT-INTERFACES, SUPPORT...). The printing pattern that corresponds to each section is indicated in Table 1. It is pointed out that auxiliary structures are not used in the G-Code for the mechanical analysis of the part because they are removed once the manufacturing process has finished.

It was shown in [49] that only the raw material properties and the infill density are required in order to fully define the constitutive behavior of the inner zone since it is mainly influenced by the geometry of the selected pattern. Therefore, the actual infill density is used to interpolate the corresponding properties of the homogenized RVE of the inner zone from a set of precomputed material tables.

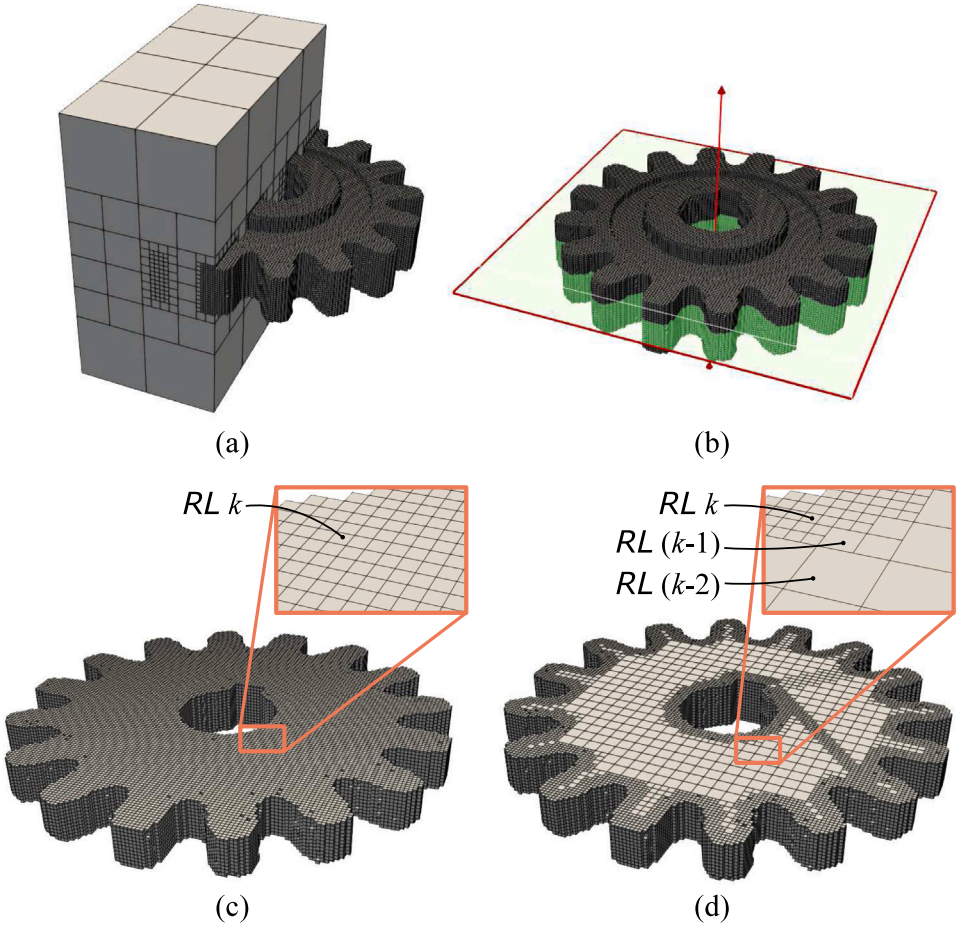

Fig. 6. Octree-based mesh strategy for a spur gear. (a) Component embedded into the bounding box. (b) Isolated component. (c) Section view of the fine mesh with 203,028 elements. (d) Section view of the coarse mesh via the octree-based strategy with 155,810 elements.

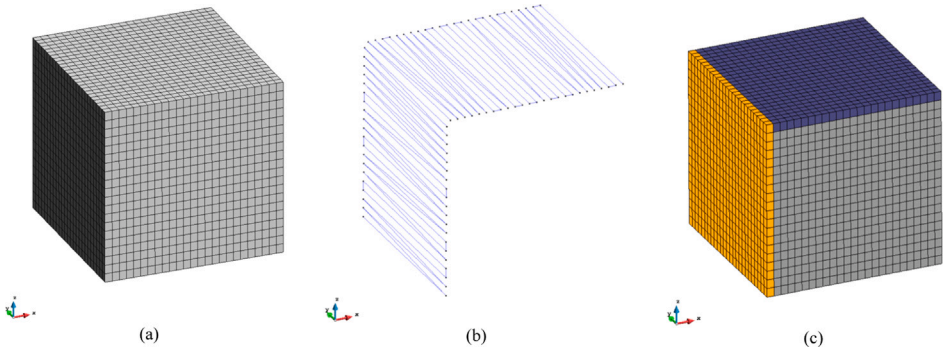

Fig. 7. BCs intersection. (a) Voxelized mesh without annotations. (b) BCs.gcode file. (c) Voxelized mesh with applied BCs (purple voxels are load constraints, while yellow voxels represent displacement constraints). (For interpretation of the references to color in this figure legend, the reader is referred to the web version of this article.)

In order to establish the likelihood of the failure of the component, the stress state of the part is mapped into a normalized scalar stress factor and then compared to a reference value. If this factor does not surpass unity, the material is said to be on the elastic range; otherwise, it is said to be in the inelastic (or plastic) range and therefore it may fail. A general orthotropic failure criterion reads [57]

$$F(\boldsymbol{\sigma}, \mathbf{f}) = \boldsymbol{\sigma}^{\mathrm{T}} \mathbf{P}_2^{\mathbf{ort}} \boldsymbol{\sigma} + \mathbf{P}_1^{\mathbf{ort}} \boldsymbol{\sigma} \leq 1 \tag{1}$$

with F being the normalized stress factor or failure function that must be less or equal to 1, σ the Voigt's representation of the symmetric second-order stress tensor and $\mathbf{f}$ an array that gathers the orthotropic material strengths $\{f_x^t,\ f_x^c,\ f_y^t,\ f_y^c,\ f_z^t,\ f_z^c,\ f_{xy},\ f_{yz},\ f_{xz}\}$, where the superscripts t and c indicate tension and compression respectively. The matrix $\mathbf{P}_2^{\mathbf{ort}}$ and the vector $\mathbf{P}_1^{\mathbf{ort}}$ are calculated as

$$\mathbf{P}_2^{\mathbf{ort}} = \begin{bmatrix} F+G & -\widetilde{F} & -\widetilde{G} & 0 & 0 & 0 \\ -\widetilde{F} & F+H & -\widetilde{H} & 0 & 0 & 0 \\ -\widetilde{G} & -\widetilde{H} & G+H & 0 & 0 & 0 \\ 0 & 0 & 0 & 2L & 0 & 0 \\ 0 & 0 & 0 & 0 & 2M & 0 \\ 0 & 0 & 0 & 0 & 0 & 2N \end{bmatrix}, \quad \mathbf{P}_1^{\mathbf{ort}} = \begin{bmatrix} I \\ J \\ K \\ 0 \\ 0 \\ 0 \end{bmatrix} \tag{2}$$

where the material parameters F, G, H, $\widetilde{F}$, $\widetilde{G}$, $\widetilde{H}$, L, M, N, I, J and K are given in terms of $\mathbf{f}$.

Multiple available failure criteria fit in this general framework depending on the way in which the above material parameters are defined: Von Mises, Drucker–Prager, Hill, Hoffman and Tsai–Wu criteria among others [57,58]. In this work, the Tsai–Wu failure criterion is applied, which is known to give reliable predictions for laminated composites with different strengths at tension and compression. For that case, the material parameters can be expressed as:

$$F = \frac{1}{2}\left[\frac{1}{f_x^t f_x^c} + \frac{1}{f_y^t f_y^c} - \frac{1}{f_z^t f_z^c}\right], \quad G = \frac{1}{2}\left[\frac{1}{f_x^t f_x^c} - \frac{1}{f_y^t f_y^c} + \frac{1}{f_z^t f_z^c}\right], \quad H = \frac{1}{2}\left[-\frac{1}{f_x^t f_x^c} + \frac{1}{f_y^t f_y^c} + \frac{1}{f_z^t f_z^c}\right] \tag{3}$$

$$\widetilde{F} = \frac{1}{2}\frac{1}{\sqrt{f_x^t f_x^c f_y^t f_y^c}}, \quad \widetilde{G} = \frac{1}{2}\frac{1}{\sqrt{f_x^t f_x^c f_z^t f_z^c}}, \quad \widetilde{H} = \frac{1}{2}\frac{1}{\sqrt{f_y^t f_y^c f_z^t f_z^c}}, \tag{4}$$

$$L = \frac{1}{2}\left(\frac{1}{f_{xy}}\right)^2, \quad M = \frac{1}{2}\left(\frac{1}{f_{xz}}\right)^2, \quad N = \frac{1}{2}\left(\frac{1}{f_{yz}}\right)^2, \tag{5}$$

$$I = \frac{1}{f_x^t} - \frac{1}{f_x^c}, \quad J = \frac{1}{f_y^t} - \frac{1}{f_y^c}, \quad K = \frac{1}{f_z^t} - \frac{1}{f_z^c}, \tag{6}$$

2.5. Optimization procedure

2.5.1. Trial analyses

In this section the approach for selecting the optimal orientation is explained in detail. Firstly, a static mechanical FE analysis is performed where the voxelized mesh, annotated with the corresponding forces and displacements BCs, and the constitutive tensors for each printing pattern are used as the input for each of the building directions that need to be studied (trials).

Because on each trial a different build orientation is simulated, the component must be rotated accordingly. However, the component rotation is equivalent to a rotation of the material constitutive tensor.

The rotation of a 6 × 6 constitutive matrix in Voigt's notation can be expressed as [59]:

$$\hat{\mathbf{C}} = \mathbf{M}^{\mathbf{T}}\mathbf{C}\mathbf{M} \tag{7}$$

where $\mathbf{C}$ refers to the original constitutive matrix and $\hat{\mathbf{C}}$ to its rotated counterpart. $\mathbf{M}$ is the rotation matrix

$$\mathbf{M} = \begin{bmatrix} A_{11}A_{11} & A_{12}A_{12} & A_{13}A_{13} & A_{12}A_{13} & A_{11}A_{13} & A_{11}A_{12} \\ A_{21}A_{21} & A_{22}A_{22} & A_{23}A_{23} & A_{22}A_{23} & A_{21}A_{23} & A_{21}A_{22} \\ A_{31}A_{31} & A_{32}A_{32} & A_{33}A_{33} & A_{32}A_{33} & A_{31}A_{33} & A_{31}A_{32} \\ 2A_{21}A_{31} & 2A_{22}A_{32} & 2A_{23}A_{33} & A_{22}A_{33}+A_{23}A_{32} & A_{21}A_{33}+A_{23}A_{31} & A_{21}A_{32}+A_{22}A_{31} \\ 2A_{11}A_{31} & 2A_{12}A_{32} & 2A_{13}A_{33} & A_{12}A_{33}+A_{13}A_{32} & A_{11}A_{33}+A_{13}A_{31} & A_{11}A_{32}+A_{12}A_{31} \\ 2A_{11}A_{21} & 2A_{12}A_{22} & 2A_{13}A_{23} & A_{12}A_{23}+A_{13}A_{22} & A_{11}A_{23}+A_{13}A_{21} & A_{11}A_{22}+A_{12}A_{21} \end{bmatrix} \tag{8}$$

with

$$A_{ij} = \cos(\hat{\mathbf{x}}_i, \mathbf{x}_j) \tag{9}$$

where $\mathbf{x}_i$ is the ith transformed axis and $\hat{\mathbf{x}}_i$ the same axis after rotation, so that

$$\hat{\boldsymbol{\sigma}} = \mathbf{M}\boldsymbol{\sigma} \tag{10}$$

After each trial simulation, the normalized stress factor field is computed using the Tsai–Wu yield criterion.

2.5.2. Selection of the build orientation

Once all the n trial orientations have been analyzed, the optimization loop starts. However, since no regression is applied, there is no continuous function to optimize and thus the conventional optimization algorithms are not applicable. In this work a statistical analysis based on the computed normalized stress factor field is performed instead.

The stress factor is defined locally, so that if the computed stress factor in a single sample point exceeds the unity, the criterion fails. The first step for obtaining the optimal orientation consists of disregarding the m trial configurations that present local failure from the total of n trial orientations. In the remaining $(n - m)$ trials the stress throughout the component is below the material strength, and then the obtention of the best configuration is not trivial. For that purpose, a representative comparison value F_c is computed for each trial, and the configuration with the lowest value is selected.

Different criteria exist depending on how F_c is computed. On the one hand, using a local criterion where the maximum stress factor of all the stress distributions is compared

$$F_c^L = \max \boldsymbol{F} \tag{11}$$

where $\boldsymbol{F} = [F_1, F_2, \ldots, F_{nodes}]$, may imply that the result is influenced by stress concentrations due to voxel artifacts along the curvature or the modeling of the load. On the other hand, using a global criterion such as an integral value computed over the whole FE mesh

$$F_c^G = \frac{\int_V F dV}{V} \tag{12}$$

may not capture the underlying physics of the problem. For these reasons, this work applies a novel selection criterion based on a Machine Learning (ML) algorithm named Anomaly Detection (AD).

AD detects patterns in data that do not show the expected behavior. These patterns are referred to as anomalies or outliers [60]. AD is extensively used in fraud detection, cyber-security and also in industrial damage detection. For the latter multiple techniques are used, being parametric statistical modeling the one applied in this work.

The general idea behind parametric statistical modeling is that the sampled data is fit into a normal distribution; points that have a very low probability to be generated are considered outliers or anomalies [61].

The training process can be summarized as, given a labeled data where each point $x \in \mathbb{R}^l$ is known in advance whether it is an anomaly or not, (i) the average and standard deviation are computed and (ii) the parameter $\varepsilon \in [0, 1]$ that maximizes the number of anomalies that fall out of the $(1 - \varepsilon)$ right confidence interval is selected. Therefore, any new point x is identified as anomalous if $P(X > x) \leq \varepsilon$. AD can be seen as a function $f : \mathbb{R}^l \rightarrow \{0, 1\}$, where 1 means anomalous and 0 non-anomalous.

This training step is not feasible for the purpose of this work since the objective is to define a general methodology and there are infinite possibilities of geometries and boundary conditions, which imply obtaining an unattainable amount of labeled data. In addition, it is not obvious if a sample point can be categorized as an anomaly or not when it does not present local failure. However, this is avoided by performing a two-step optimization. Looking for the best orientation among the specified possibilities, a more "qualitative" comparison can be made. Hence it is not necessary to identify the anomalies, but to select the orientation with the least number of anomalies.

Since the generation of a training data set or a model is not possible, the AD technique is adapted in the following way. First, the stress factor field of each trial orientation is fit into a normal distribution, and the right 5% confidence interval $F_c^{95\%}$ is computed:

$$F_c^{95\%} = F_c^G + z_{95\%}\sigma \tag{13}$$

where σ is the standard deviation of the distribution and $z_{95\%}$ the value of a normal distribution with mean 0 and standard deviation 1 ($Z \sim \mathcal{N}(0, 1)$) such that $P(Z < z_{95\%}) = 0.95$.

The objective of the algorithm is reducing the number of stresses higher than this right confidence interval, defining those as anomalies. However, the number of anomalies present in a distribution depends on the used confidence interval. If each distribution's respective confidence interval is used, all distributions end up with the same number of anomalies. Therefore, the proper approach is computing, for each distribution, its number of outliers considering the confidence intervals of all distributions except its own.

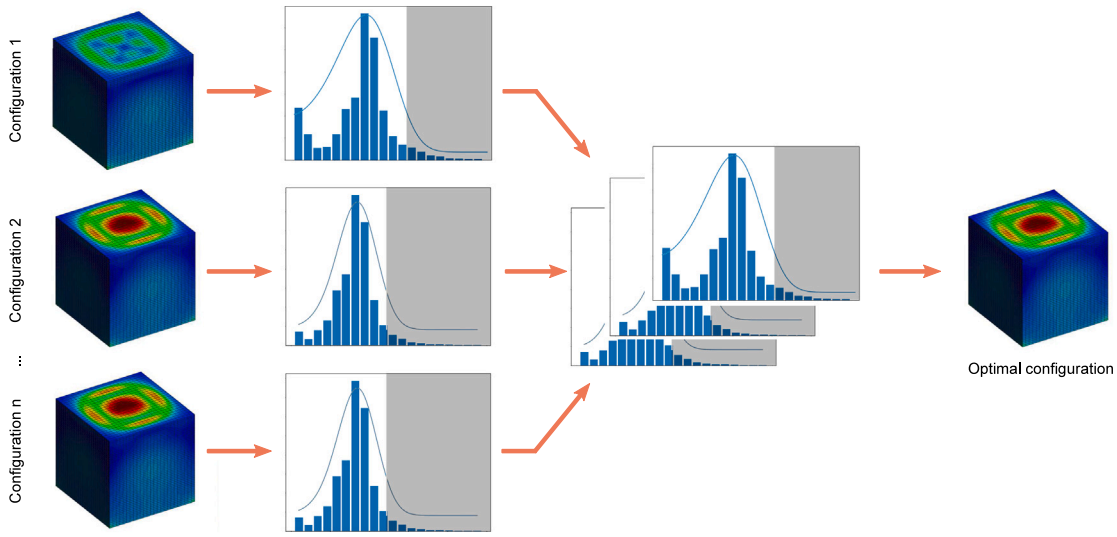

Fig. 8. Developed statistical criterion based on AD.

Finally, it is selected as optimal the trial configuration that, when using its $F_c^{95\%}$ as a reference, makes the other configurations have the highest number of anomalies. This is equivalent to select as optimal the trial configuration with the lowest $F_c^{95\%}$. The process is depicted in Fig. 8 and summarized in Algorithm 2.

Algorithm 2: Selection of the build direction based on the statistical criterion

Data: The set of stress factor distributions $\boldsymbol{F}_i \in \mathbb{R}^{nodes}$ from all the trial orientations: $[\boldsymbol{F}_1, \boldsymbol{F}_2, ..., \boldsymbol{F}_{n-m}]$
Result: The optimal orientation $d \in \mathbb{N}$

for $i = 1$ *to* $(n - m)$ **do**
  $\mu_i, \sigma_i \leftarrow$ Average and standard deviation of $\boldsymbol{F}_i$
  $F_c^{95\%} \leftarrow \mu_i + z_{95\%} \cdot \sigma_i$ /* where $z_{95\%} = 1.655$ */
  $\boldsymbol{F}_c \leftarrow \boldsymbol{F}_c \cup F_c^{95\%}$
$d \leftarrow i$ such that $\min_i \boldsymbol{F}_{\boldsymbol{c},i}$

3. Test cases

In this section some numerical examples illustrate the performance of the proposed methodology without the octree-based coarsening. The objective is to validate the presented methodology with test cases whose output can be easily analyzed. However, it is applicable to more complex loading conditions since the FE analysis is performed in a linear elastic regime, and therefore any complex loading condition can be expressed as a superposition of simple cases. PLA is the used material and its properties [48] are shown in Tables 2 and 3, where x and y denote the axes contained in the horizontal (printing) plane and z is the vertical (printing) direction. The shell properties are assigned to the G-Code zones labeled as WALL-INNER, WALL-OUTER and SKIN in Table 1, while the infill properties are to the FILL zones.

Two test cases are presented. The first one demonstrates the robustness of the novel statistical criterion based on the ML algorithm AD. The second example shows the validity of the voxelized approach against experimental results as well as the comparison with the classical methodology based on an STL file.

A high number of orientations can be analyzed since each simulation takes a few seconds. For demonstrative purposes 3 orientations are simulated in all the test cases: the default build direction (Orientation 1), one with a rotation of 90°around the X axis (Orientation 2) and another with a 90°rotation around the Y axis (Orientation 3).

The numerical simulations are performed using the in-house software COMET [62] developed by the authors at the International Center for Numerical Method in Engineering (CIMNE) in Barcelona, Spain. The post-processing is done using the pre and post-processor GiD [63] also developed at CIMNE.

Table 2
Material properties for PLA.

	E_x (GPa)	E_y (GPa)	E_z (GPa)	G_{xy} (GPa)	G_{yz} (GPa)	G_{xz} (GPa)	ν_{xy}	ν_{zy}	ν_{zx}
Shell	1.98	1.98	2.32	0.73	0.63	0.63	0.35	0.35	0.35
50% Infill	0.20	0.20	1.53	0.44	0.39	0.39	0.81	0.24	0.24

Table 3
Material strengths for PLA. Units in MPa.

	f_x^t	f_x^c	f_y^t	f_y^c	f_z^t	f_z^c	f_{xy}	f_{yz}	f_{xz}
Shell	25.13	28.83	25.13	28.83	18.22	47.83	15.54	7.77	7.77
50% Infill	12.57	14.42	12.57	14.42	9.11	23.92	7.77	3.89	3.89

3.1. Cantilever beam

This test-case demonstrates how the decision on the optimal build direction is affected by the way in which the load is applied due to the presence of stress concentrators or singularities. With the novel statistical criterion, the selected direction is the same regardless of how the load is applied. This robustness is not obtained for other criteria.

The dimensions of the cantilever beam in its original build orientation as well as the two different types of applied load are reported in Fig. 9. The beam is clamped at one end and subjected to a vertical load at the opposite end. For case 1, the load is applied as a pressure of 0.2 MPa over a 50 mm^2 surface, while for case 2 it is a 10 N point load. A voxelized mesh with eight-noded hexahedral elements is used to obtain the solution with a voxel size of $0.4 \times 0.4 \times 0.2$ mm^3.

Fig. 10 compares the magnitudes of the computed stress factors using the Tsai–Wu yield criterion for the volumetric and point load cases in the three different build directions. In each plot the location of the maximum value is indicated.

When the volumetric load is applied, the maximum values of the stress factor are located near the clamping. However, for the point load cases, the maximum values appear on the application point of the load. The only sample points where the stress factor is above unity are due to the stress concentrations caused by the point load and, thus, no configuration presents local failure.

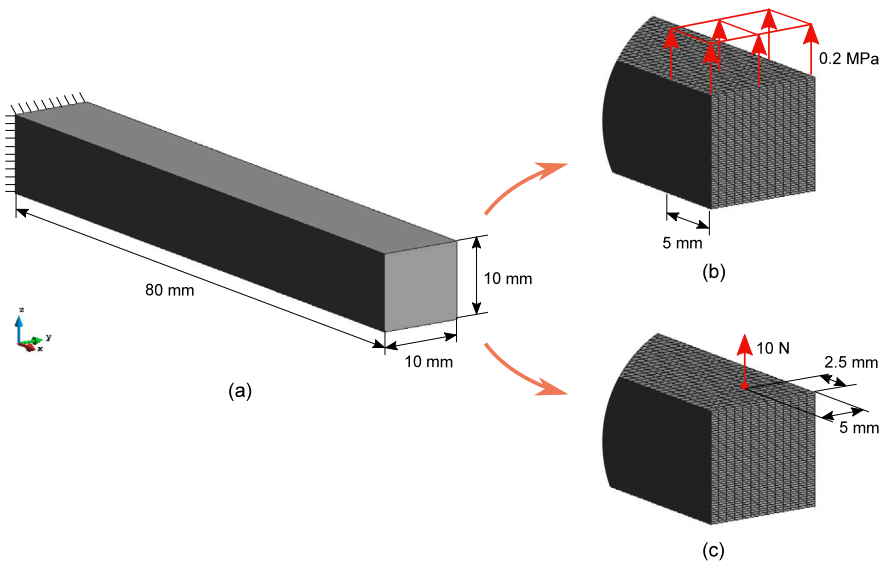

Fig. 9. Cantilever beam problem definition. (a) General dimensions. (b) Applied volumetric load. (c) Applied point load.

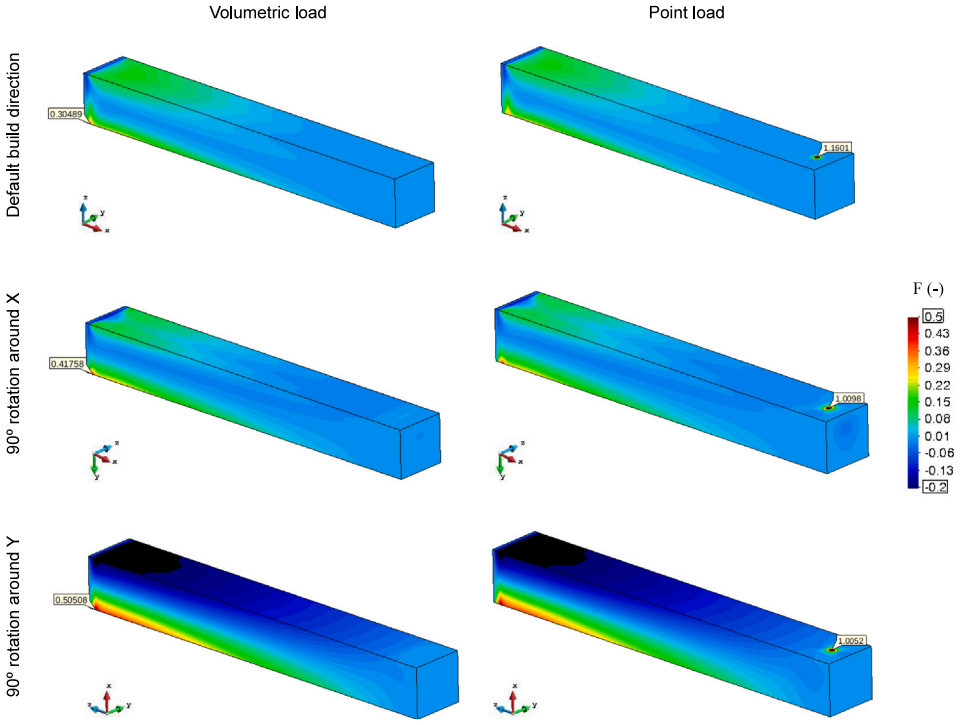

Fig. 10. Cantilever beam: Stress factors for the point and volumetric loads in the 3 simulated build directions.

The stress factor distribution of each orientation do not closely follow a normal distribution. In order to approximate them as such, a Box–Cox transformation [64] has been applied to each F_i such that

$$F_i = (F_i^{\lambda} - 1)/\lambda \tag{14}$$

where λ is a parameter that is chosen for maximizing the resemblance of the data to a normal distribution. This transformation is only used for visualization purposes. The transformed stress factor distribution as well as the probability density function of each case are shown in Fig. 11, where the shaded area indicates the 5% upper tail of the distribution. The X axes have been scaled for the sake of clarity.

Each distribution has a different optimal value of λ. The average optimum of all the 6 configurations, $\lambda = -0.3$, has been selected for Eq. (14).

The distributions of the stress factor show similar trends for both the volumetric and point load cases in orientations 1 and 2, but not so for orientation 3, where a flatter and wider distribution can be seen; also, the highest noticeable values for both cases in orientation 3 are higher than in orientations 1 and 2.

However these plots are mainly qualitative and a more deterministic way for electing the optimal orientation is required. That is the reason why the statistical criterion is used. In the following, a comparison between the statistical criterion and a maximum (local) and an average (global) stress criteria is made. The F_c values of the analyzed cases are shown in Table 4. The green background indicates the optimal orientation, while the red background relates to the worst orientation for each respective criterion.

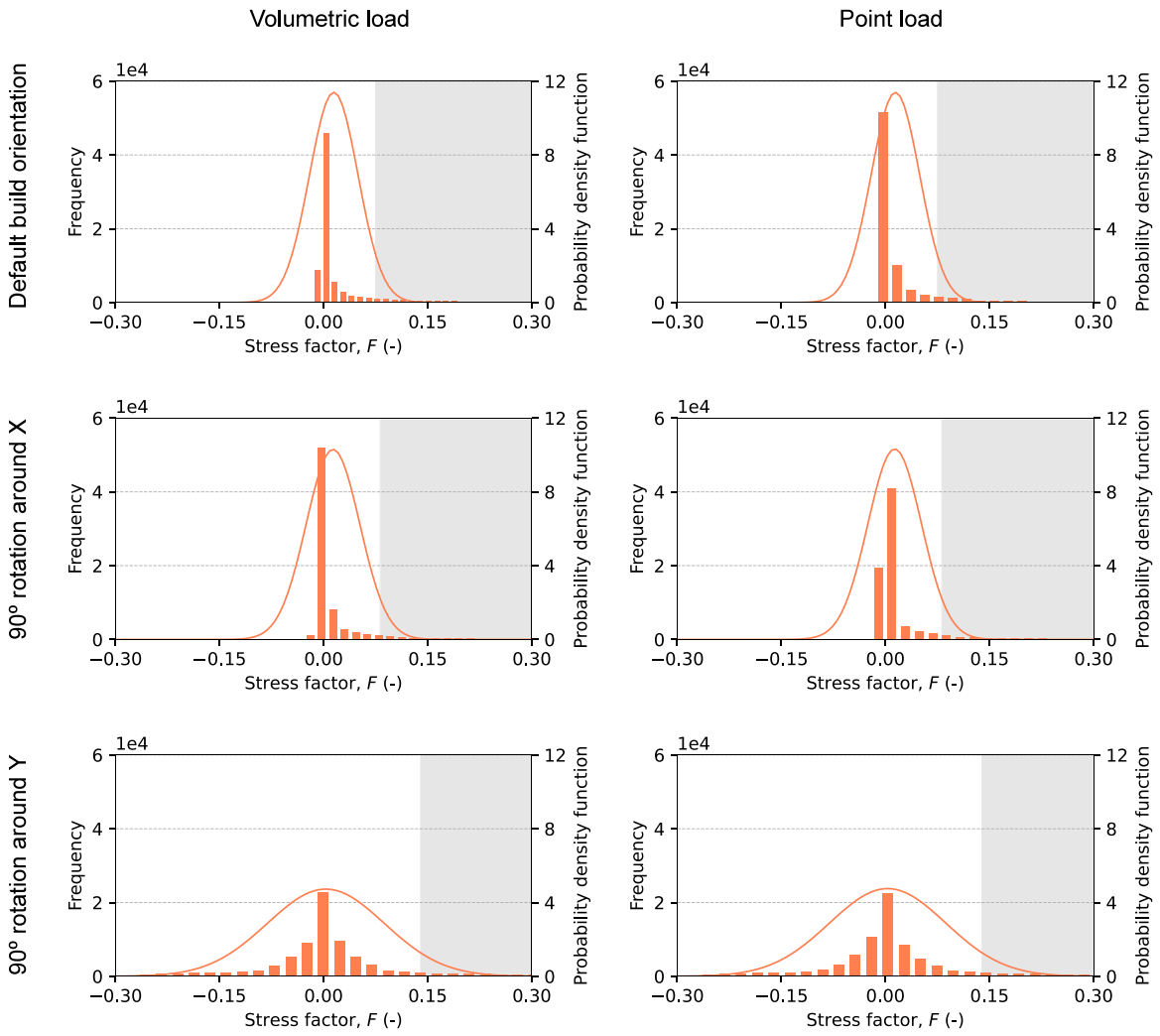

Fig. 11. Cantilever beam: Stress factor distribution for the point and volumetric loads in the 3 simulated build directions.

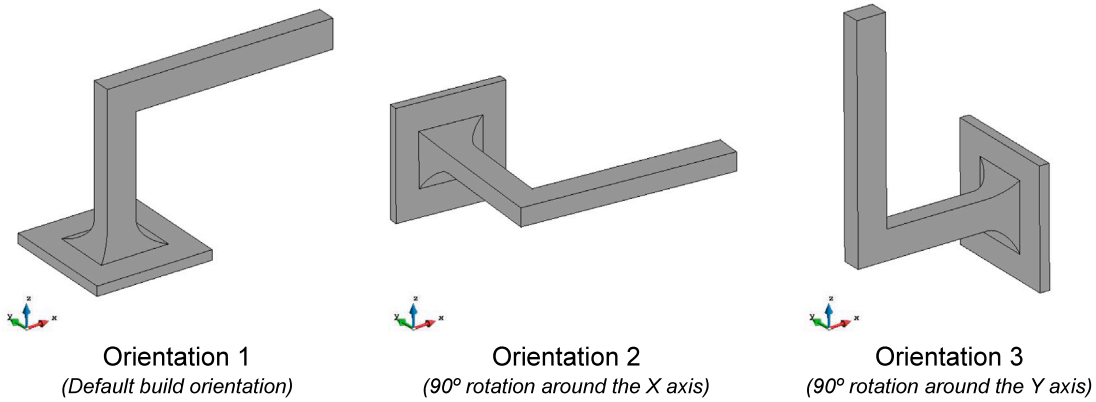

Fig. 12. Door handle printed orientations.

For the maximum criterion, when a volumetric load is considered, the lowest maximum value of the stress factor is obtained in orientation 1, which coincides with the solution from the statistical criterion, while for the point load case this agreement is lost. The average criterion recommends orientation 3 for both the volumetric and point loads, which differs from the statistical approach. The worst printing orientation indicated by the statistical criterion is orientation 3 (the beam is printed vertically), independently on the applied load, as expected.

On the one hand, the maximum criterion is very much affected by the way in which the load and support conditions are modeled in the

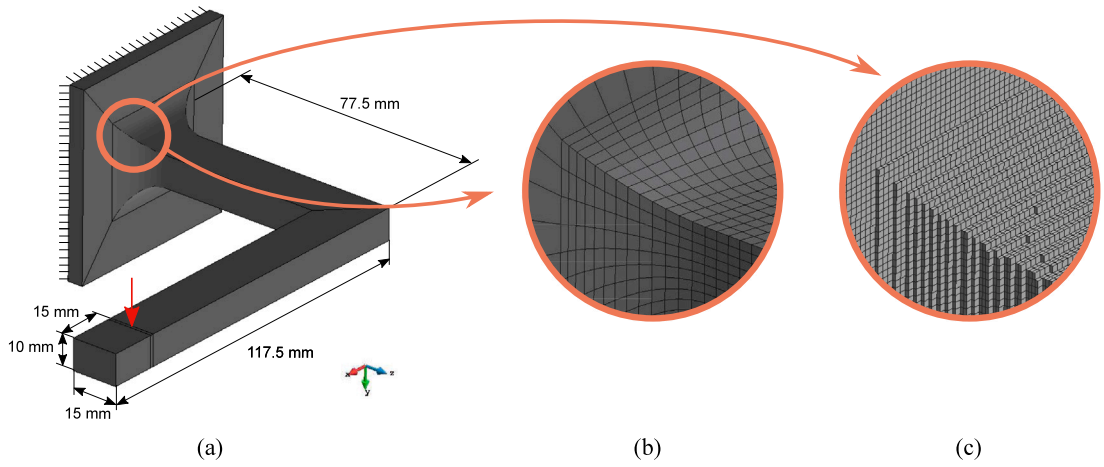

Fig. 13. Door handle test-case. (a) Geometry and boundary conditions. (b) STL mesh. (c) Voxelized mesh.

Table 4
F_c values for the volumetric and point load cases of the cantilever beam in the 3 build orientations.

		Orientation 1	Orientation 2	Orientation 3
Volumetric	F_c^L (-)	0.297	0.423	0.514
	F_c^G (-)	0.016	0.015	0.008
	$F_c^{95\%}$ (-)	0.079	0.086	0.150
Point	F_c^L (-)	1.164	1.012	1.008
	F_c^G (-)	0.016	0.015	0.008
	$F_c^{95\%}$ (-)	0.079	0.086	0.151

FE models. On the other hand, the average criterion fails in describing the problem and does not capture the geometrical and physical complexities of the case. The statistical criterion is able to describe the actual stress state of the component in a more comprehensive way and is undoubtedly the most robust one.

3.2. Door-handle

The second test-case corresponds to a door-handle demonstrator. This example shows the validity of the model against experimental results as well as a comparison of the optimal build orientation calculation between a simulation with the classical STL input file and the novel voxelized approach. The comparison between the experimental and the simulation results is made analyzing their linear elastic behavior shown in their respective load–displacement curves.

The 3 printed orientations of the component are shown in Fig. 12 and their main dimensions are depicted in Fig. 13(a). The component is printed with double outer shell thickness and the in-fill type is rectilinear with ±45°raster angle.

For the experimental tests the structure is clamped at one end and the loading consists of a vertical displacement of 35 mm applied at a distance of 15 mm from the end of the door-handle at a loading speed of 1 mm/min. Note that the door-handle is subjected to bending and torsion, and complex stress states need to be accurately captured by the FE computations.

For the simulation, a vertical load of 15 N is used. The computational domain is discretized with eight-noded hexahedral elements. On the one hand, for the structured mesh obtained from the STL file an average element size of h = 1.5 mm is used for the handle, while a coarser element size of h = 6 mm is selected for the clamped base (Fig. 13(b)). On the other hand, the voxelized mesh elements are again characterized by a size of 0.4 × 0.4 × 0.2 mm^3 (Fig. 13(c)).

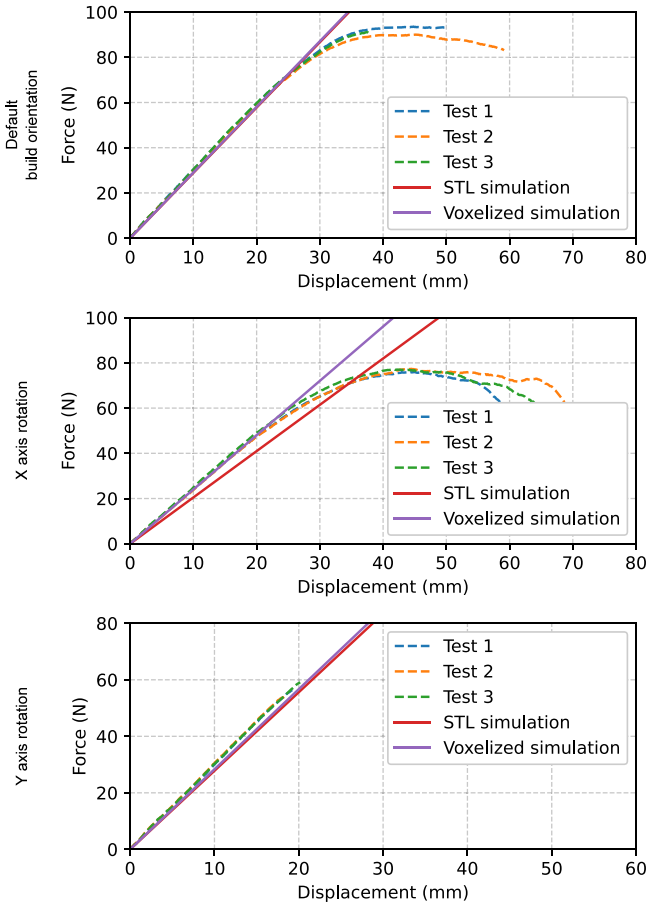

Fig. 14. Door handle force–displacement curves for the experiments and the simulations with the STL and voxelized geometries in the 3 different orientations.

The three force–displacement curves of each printed orientation are shown in Fig. 14. Very good agreement is found between the experimental and the computational results. Even though the STL-based methodology shows a great similitude to the experiments, the voxelized approach greatly improves it and presents a much lower difference with the experimental data, as can be clearly perceived for orientation 2. The reason for this is the greater resemblance to the actual geometry that the voxelized mesh has since it is directly obtained from the G-Code and

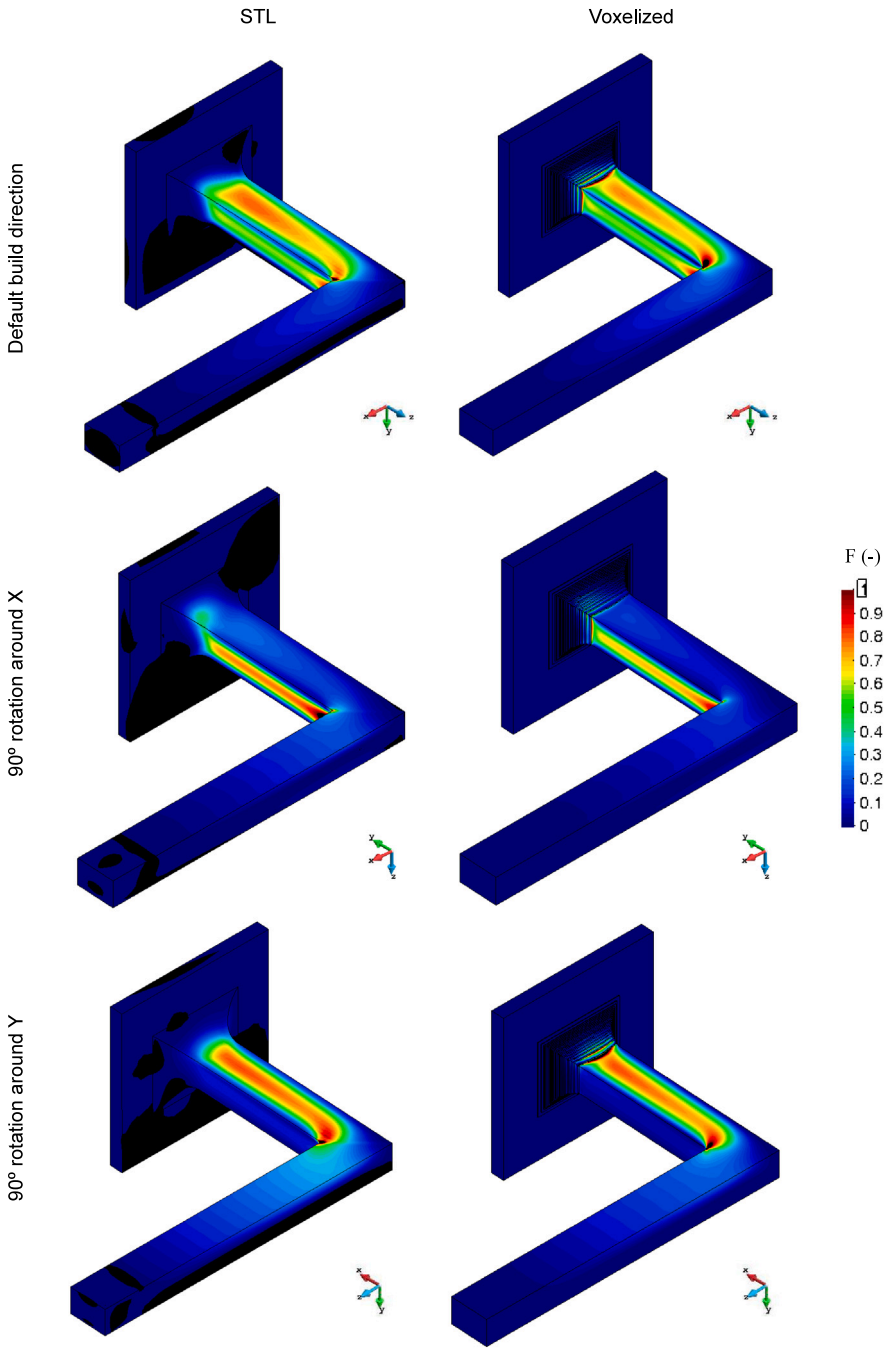

Fig. 15. Door handle: Stress factors results for the STL and voxelized geometries in the 3 simulated build directions.

therefore it includes small manufacturing details such as the different layers or tiny deviations from the shape of the as-designed component.

In the experiments, all orientations exhibit a similar structural behavior, being orientation 3 the only one that shows a brittle type of fracture.

Fig. 15 shows the stress factor fields for the STL and voxelized meshes in the three simulated directions. The maximum values of all the cases are below unity and are located in the shell zone as it follows under bending and torsion stress. More specifically, the most stressed areas are all located at the 90°corner of the handle, which is the zone where the printed components broke as shown in Fig. 16. Therefore, no orientation presents local failure.

The obtained stress factors lay on a similar range for both the STL and voxelized approaches, being slightly higher in the latter. It is remarkable the fact that in orientation 2 the vertical (YZ) surface near the clamping is the zone with maximum stress factors, while in orientation 3 it is the horizontal (XZ) surface. This is explained due to the orthotropic nature of the material. In orientation 2 the strength for the vertical (YZ) surface corresponds to the in-plane shear strength ($f_{yz} = 7.77$ MPa), which is much lower than the traverse shear strength ($f_{xz} = 15.54$ MPa), resulting in a higher value of F based on Eq. (1). In contrast, in orientation 3 it is the horizontal (XZ) surface the one characterized by the transverse shear strength f_{xz}. This phenomenon can also be seen in orientation 1. However, in that case the stress factors in both surfaces are equal since they are both defined by the traverse shear strength f_{xz}.

Fig. 17 shows the stress factors distribution of the analyzed cases and Table 5 their respective $F_c^{95\%}$ values. This time no Box-cox transformation has been applied to the distributions since it did not improve their visual resemblance to a normal distribution.

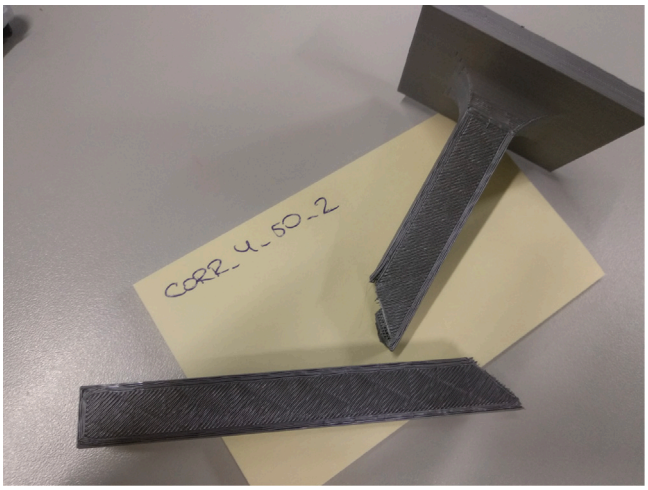

Fig. 16. Broken door handle from orientation 2.

Table 5
F_c values for the STL and voxelized cases of the door-handle in the 3 build orientations.

		Orientation 1	Orientation 2	Orientation 3
STL	F_c^L (-)	3.461	1.108	3.202
	F_c^G (-)	0.054	0.026	0.048
	$F_c^{95\%}$ (-)	0.276	0.140	0.233
Voxelized	F_c^L (-)	3.529	1.347	2.242
	F_c^G (-)	0.035	0.022	0.034
	$F_c^{95\%}$ (-)	0.189	0.131	0.178

The biggest difference between histograms is that the relative frequencies for $F \approx 0$ in the STL case are lower than in the voxelized approach. This is due to the difference of the element sizes in the STL mesh, where a bigger element size is used near the clamping zone. In order to take that into account, the frequencies should be scaled according to the element volume, which is not considered in the plot. As seen in Fig. 15, the value of the stress factors in the clamping are lower than in the handle. This is the reason why this phenomenon is more noticeable for the frequencies where the stress factor approaches 0.

All the F_c values coincide in both approaches and indicate that the optimal build direction is orientation 2 (application of a 90°rotation around the X axis to the original build configuration). Moreover, all the criteria indicate that orientation 1 is the worst one, which is, in turn, the orientation that minimizes the amount of support structure. The reason for this is that the zone of the handle near the clamping is under bending and torsion, while the far off part is only under a bending. Thus, the near zone is under higher solicitations as shown in Fig. 15, and therefore the orientation in which this zone is vertically printed (orientation 1) is the less favorable one.

4. Case study

In this section an industrial case with a complex geometry is solved. The optimal orientation of a prosthetic finger made of PLA is determined using the octree-based mesh strategy, showing that the proposed strategy is also applicable to the manufacturing of medical devices.

The 3 simulated printed orientations of the component are shown in Fig. 18. The main dimensions of the prosthesis and the applied boundary conditions are depicted in Fig. 19(a). The prosthesis is fixed at the two end holes and it is subjected to a vertical 50 N load uniformly distributed at the opposite end. The resulting octree-based mesh is shown in Fig. 19(b) and (c), where a maximum RL of 7 has been used. The discrete domain is constructed from a bounding box

Table 6
F_c values of the loaded prosthesis in the 3 build orientations.

	Orientation 1	Orientation 2	Orientation 3
F_c^L (-)	0.373	0.671	0.389
F_c^G (-)	0.007	0.004	0.007
$F_c^{95\%}$ (-)	0.046	0.095	0.041

of dimensions 54.2 × 54.2 × 54.2 mm^3, resulting in voxels of size 0.4234 × 0.4234 × 0.4234 mm^3 at RL 7.

Fig. 20 shows the stress factor fields for the 3 different printing orientations. The maximum values in all the cases are below unity. The most stressed zones are all located in the shell due to the geometry. Despite the apparent complexity of the component, it can be seen as a cantilever beam mainly subjected to bending, with the highest stresses near the surface. All the orientations lie in the elastic range and therefore the optimization loop is applicable to all of them.

Fig. 21 shows the stress factor distribution of the analyzed cases. Orientation 2 shows a slightly more plane and different behavior, with higher frequencies for higher stresses values. This can also be seen in the results from Table 6, where it is the worst orientation according to the maximum (local) and statistical criteria.

Table 6 shows the F_c values for all the build directions. It should be noted that now the elements have a variable size due to the octree-based strategy used. Therefore the stress factor from an element belonging to RL6 has 8 times more frequency than one from RL7. When computing the volume average of F this phenomena is implicitly taken into account. In order to also consider it when obtaining the 95% confidence interval a weighted standard deviation is used

$$\sigma_w = \sqrt{\frac{\sum_{i=1}^{N} w_i (x_i - \overline{x}^*)^2}{\frac{N-1}{N} \sum_{i=1}^{N} w_i}} \tag{15}$$

where N refers to the number of sample points, w_i to the weight of point i (calculated as the volume fraction of the voxel) and $\overline{x}^*$ is the weighted mean of the distribution obtained via the volume average. The confidence interval is calculated replacing σ with σ_w in Eq. (13).

The results from the statistical criterion indicate that orientation 3 is the optimal printing direction, while the maximum (local) criterion states that the most suitable configuration is orientation 1. However, as shown in the first example, the local criterion does not show the robustness of the parametric statistical analysis from AD, and thus it can be drawn that orientation 3 is the optimal build direction. As for the cantilever beam from Section 3.1, the vertically printed component presents the worst mechanical performance as expected. It should be noted that this vertically printed orientation minimizes the amount of support structure, which implies that a decision must be made between optimizing the mechanical performance or reducing the material waste. Again, the average (global) criterion fails in describing the physical complexities of the problem, indicating that orientation 2 is the most suitable printing direction.

Fig. 22 shows graphically the efficiency of the used strategy. The left plot indicates that the computational cost of the mesh generation using the octree-based strategy is much higher than using the fine mesh approach. However, this methodology outputs a coarser mesh that results in significant savings in the simulation time. This can be clearly seen in the right plot where, despite the initial cost of the creation of the octree-based mesh, the more number of orientations that are simulated, the more efficient the strategy becomes.

5. Conclusions

In this work, a novel end-to-end solution for the optimization of the performance of ME components is presented. This methodology includes from the G-Code file generation to the manufacturing of the actual component. An octree-based mesh is generated from the manufacturing toolpaths and FE simulations are performed under user-defined

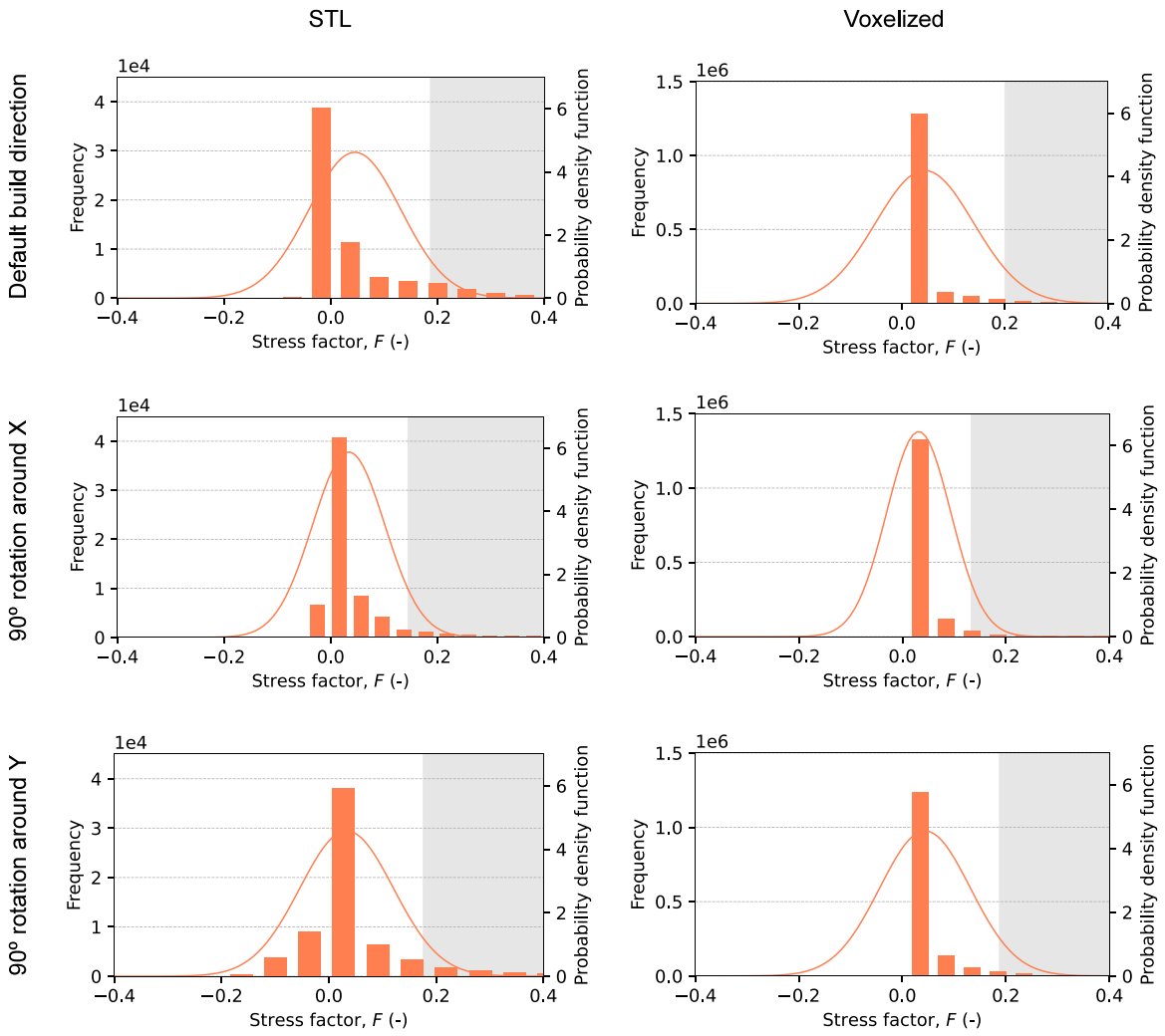

Fig. 17. Door handle: Stress factors distribution for the STL and voxelized geometries in the 3 simulated build directions.

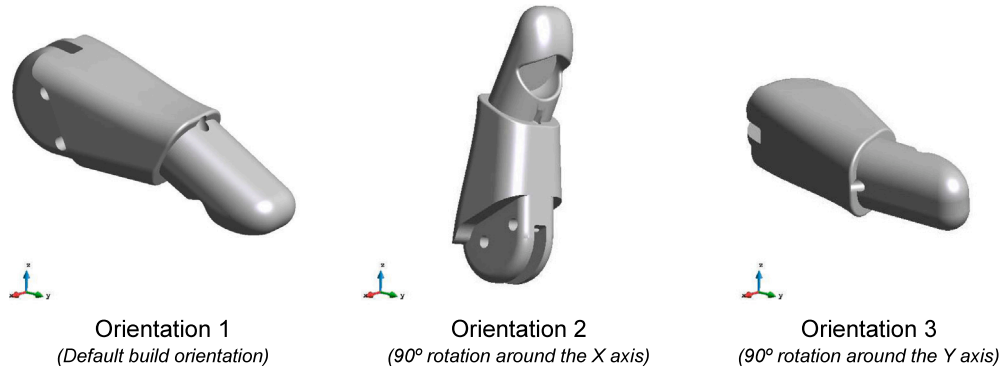

Fig. 18. Prosthetic finger printed orientations.

conditions. A two-step optimization on the results drives the decision on the optimal build direction regarding mechanical performance.

From the analyses of the presented test cases it is concluded that the proposed statistics-based optimization criterion is an appropriate choice regarding geometrical and mechanical complexities, as well as robustness with respect to the FE discretizations of load and support conditions. As shown in the door-handle demonstrator, the voxelization approach based on the G-Code file not only avoids the use of a STL file and its resulting drawbacks, but also improves the accuracy of the results compared to the experiments due to its major resemblance to the actual geometry compared to the STL-based methodology. The coarsening of the mesh via the octree-based strategy significantly reduces the computational cost of the FE simulations, which allows for the scalability of the strategy to more complex industrial cases.

A significant advantage of this optimization technique is that it can also be extended to different AM technologies apart from ME with very

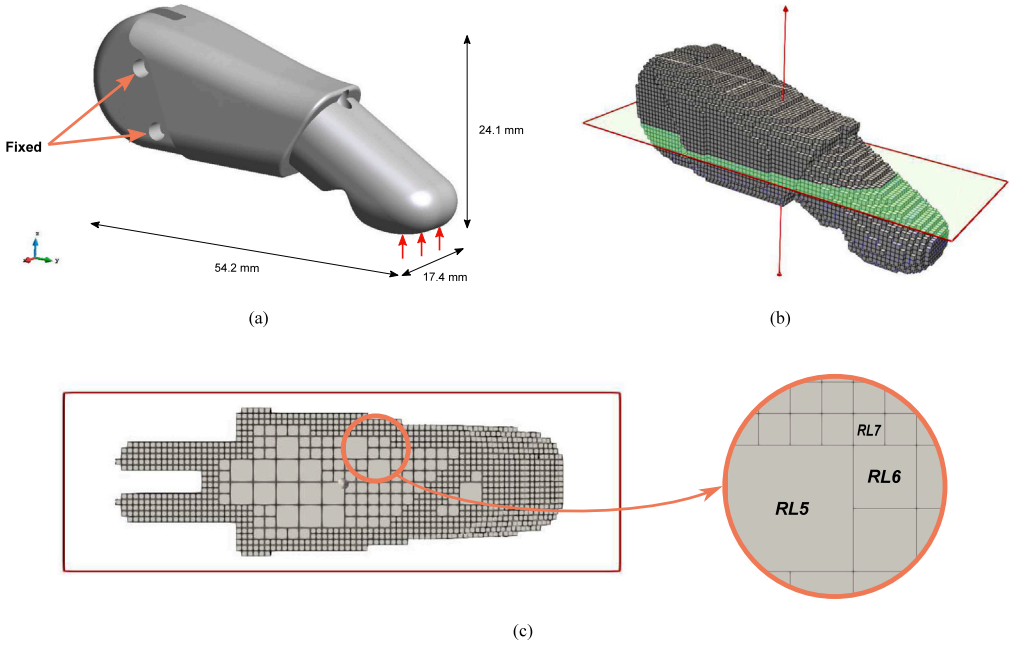

Fig. 19. Prosthetic finger: (a) Geometry and boundary conditions. (b) Resulting octree-based mesh. (c) Cross-section view and RLs.

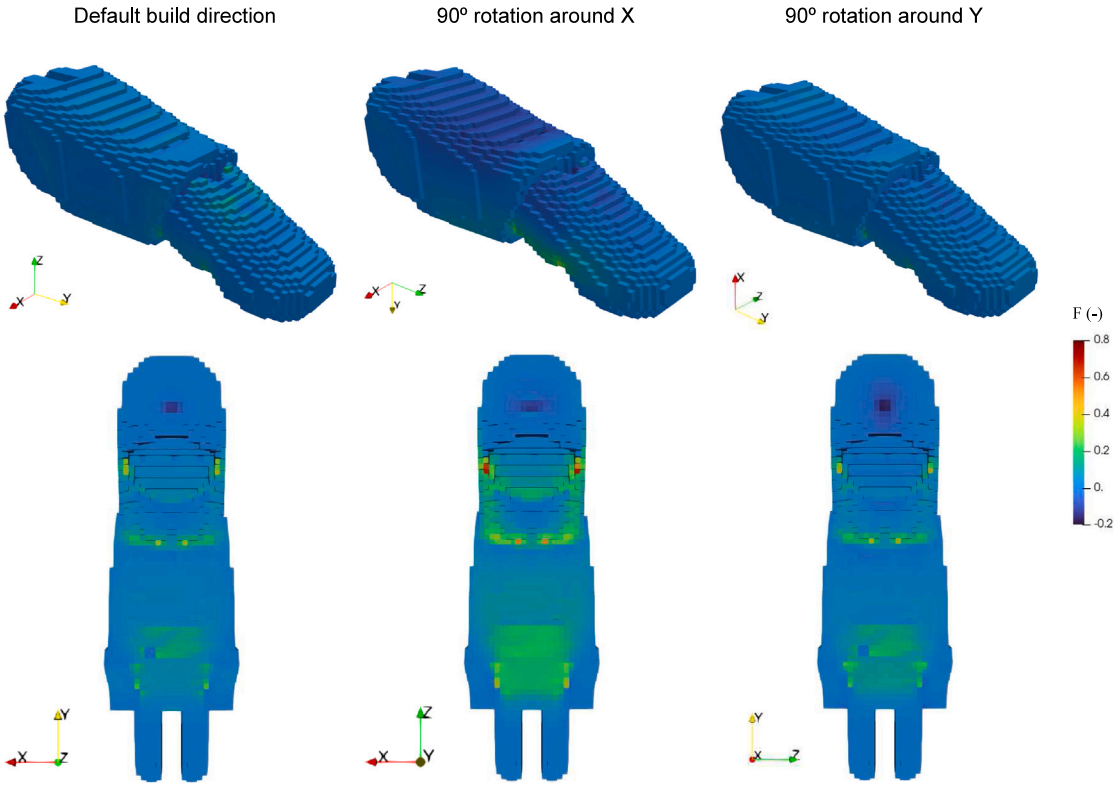

Fig. 20. Prosthetic finger: stress factors results in the 3 simulated build directions.

minor adjustments, such as the material model and the failure criterion appropriate to the analyzed AM process and material.

Two-step optimization methods may miss the true optimal build direction for complex cases since only a set of orientation candidates are analyzed. However, this methodology is more efficient because it avoids the computation of a large number of meaningless orientations and always gives a near-optima solution.

Future improvements and applications of this work will address a Multi Criteria Decision Making (MCDM) for the optimization of other process parameters such as the minimization of the material consumption or the printing time. In addition, the analysis of complex topologies such as lattice or organic structures under more complex loading conditions is a potential future research line. The study of fracture mechanics by expanding the presented constitutive model to nonlinear damage analysis is also to be carried out.

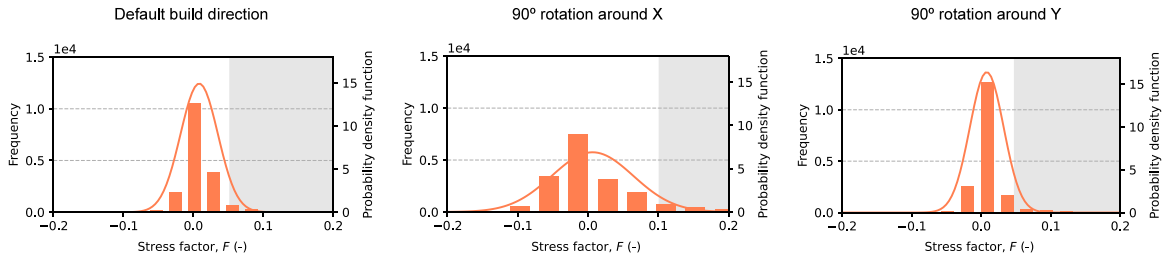

Fig. 21. Prosthetic finger: stress factor distribution in the 3 simulated build directions.

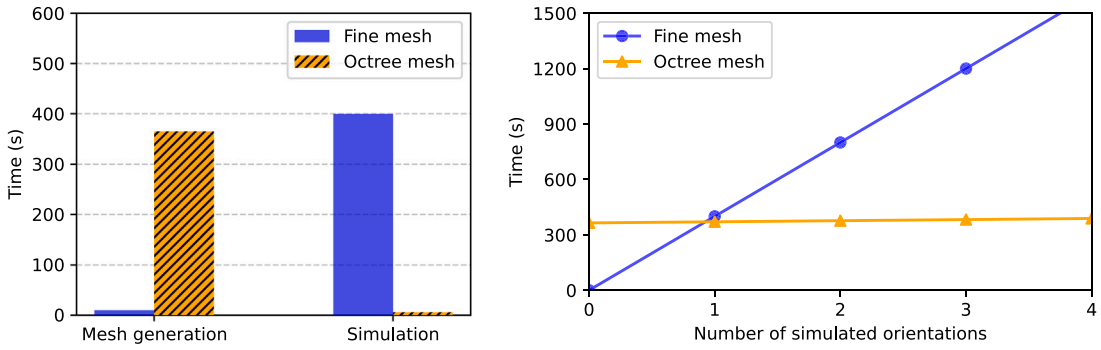

Fig. 22. Prosthetic finger: Efficiency of the fine and the octree-based meshes. Comparison of the CPU time between the mesh generation and the simulation (left) and variation of the CPU time of the whole optimization procedure with respect to the number of analyzed orientations (right).

CRediT authorship contribution statement

Iván Rivet: Writing – review & editing, Writing – original draft, Software, Methodology, Investigation, Data curation. **Narges Dialami:** Writing – review & editing, Supervision, Software, Methodology, Conceptualization. **Miguel Cervera:** Writing – review & editing, Supervision, Software, Project administration, Funding acquisition, Conceptualization. **Michele Chiumenti:** Writing – review & editing, Software, Project administration, Methodology, Funding acquisition, Formal analysis. **Quino Valverde:** Resources, Data curation.

Declaration of competing interest

The authors declare that they have no known competing financial interests or personal relationships that could have appeared to influence the work reported in this paper.

Data availability

Data will be made available on request.

Acknowledgments

This work has been supported by the European Union's horizon 2020 research and innovation programme (H2020-DT-2019-1 No. 872570) under the KYKLOS 4.0 Project (An Advanced Circular and Agile Manufacturing Ecosystem based on rapid reconfigurable manufacturing process and individualized consumer preferences) and by the Ministry of Science, Innovation and Universities (MCIU) via: the PriMuS project (Printing pattern based and MultiScale enhanced performance analysis of advanced Additive Manufacturing components, ref. num. PID2020-115575RB-I00).

The financial support from the Spanish Ministry of Economy and Competitiveness, through the Severo Ochoa Programme for Centres of Excellence in R&D (CEX2018-000797-S), is gratefully acknowledged as well as from CONCYTEC R+D (Project Reference: 163-2017-FONDECYT, in association with Pontifical Catholic University of Perú and CIMNE) - "Optimización del uso de polímeros sintéticos en procesos de manufactura aditiva mediante modelos de simulación computacional *y* técnicas de caracterización de materiales. Caso de estudio: aplicaciones médicas - prótesis de mano". Narges Dialami is a Serra Húnter fellow.

References

[1] J. Jiang, Y. Ma, Path planning strategies to optimize accuracy, quality, build time and material use in additive manufacturing: A review, Micromachines 11 (7) (2020) http://dx.doi.org/10.3390/mi11070633.

[2] Jingchao J., A novel fabrication strategy for additive manufacturing processes, J. Clean. Prod. 272 (2020) 122916, http://dx.doi.org/10.1016/j.jclepro.2020.122916.

[3] T.D. Ngo, A. Kashani, G. Imbalzano, K.T.Q. Nguyen, D. Hui, Additive manufacturing (3D printing): A review of materials, methods, applications and challenges, Composites B 143 (2018) 172–196, http://dx.doi.org/10.1016/j.compositesb.2018.02.012.

[4] E. Cuan-Urquizo, E. Barocio, V. Tejada-Ortigoza, R. Pipes, C. Rodriguez, A. Roman-Flores, Characterization of the mechanical properties of FFF structures and materials: A review on the experimental, computational and theoretical approaches, Materials 12 (6) (2019) 895, http://dx.doi.org/10.3390/ma12060895.

[5] J. Jiang, Y.F. Fu, A short survey of sustainable material extrusion additive manufacturing, Aust. J. Mech. Eng. (2020) 1–10, http://dx.doi.org/10.1080/14484846.2020.1825045.

[6] J. Jiang, X. Xu, J. Stringer, Optimization of process planning for reducing material waste in extrusion based additive manufacturing, Robot. Comput.-Integr. Manuf. 59 (2019) 317–325, http://dx.doi.org/10.1016/j.rcim.2019.05.007.

[7] S.D. Nath, S. Nilufar, An overview of additive manufacturing of polymers and associated composites, Polymers 12 (11) (2020) http://dx.doi.org/10.3390/polym12112719.

[8] M. Harris, J. Potgieter, R. Archer, K.M. Arif, Effect of material and process specific factors on the strength of printed parts in fused filament fabrication: A review of recent developments, Materials 12 (10) (2019) 1664, http://dx.doi.org/10.3390/ma12101664.

[9] D.W. Holmes, D. Singh, R. Lamont, R. Daley, D.P. Forrestal, P. Slattery, E. Pickering, N.C. Paxton, S.K. Powell, M.A. Woodruff, Mechanical behaviour of flexible 3D printed gyroid structures as a tuneable replacement for soft padding foam, Addit. Manuf. 50 (2022) 102555, http://dx.doi.org/10.1016/j.addma.2021.102555.

[10] S.C. Ligon, R. Liska, J. Stampfl, M. Gurr, F. Mülhaupt, Polymers for 3D printing and customized additive manufacturing, Chem. Rev. 117 (15) (2017) 10212–10290.

[11] A.B. Stefaniak, L.N. Bowers, G. Cottrell, E. Erdem, A.K. Knepp, S.B. Martin, J. Pretty, M.G. Duling, E.D. Arnold, Z. Wilson, B. Krider, A.R. Fortner, R.F. LeBouf, M.A. Virji, A. Sirinterlikci, Towards sustainable additive manufacturing: The need for awareness of particle and vapor releases during polymer recycling, making filament, and fused filament fabrication 3-D printing, Resour. Conserv. Recy. 176 (2022) 105911, http://dx.doi.org/10.1016/j.resconrec.2021.105911.

[12] L. Li, R. McGuan, R. Isaac, P. Kavehpour, R. Candler, Improving precision of material extrusion 3D printing by in-situ monitoring & predicting 3D geometric deviation using conditional adversarial networks, Addit. Manuf. 38 (2021) 101695, http://dx.doi.org/10.1016/j.addma.2020.101695.

[13] I.S.O. 6983 International Standards Organization, Automation Systems and Integration — Numerical Control of Machines — Program Format and Definitions of Address Words — Part 1: Data Format for Positioning, Line Motion and Contouring Control Systems, 2005.

[14] S. Shin, S. Suh, I. Stroud, Reincarnation of G-code based part programs into STEP-NC for turning applications, Comput. Aided Des. 39 (1) (2007) 1–16, http://dx.doi.org/10.1016/j.cad.2006.08.005.

[15] Simplify home page, 2022, https://simplify3d.com. (Accessed 10 November 2022).

[16] Slic3r home page, 2022, https://slic3r.org. (Accessed 10 November 2022).

[17] D. Zhao, W. Guo, Shape and performance controlled advanced design for additive manufacturing: A review of slicing and path planning, J. Manuf. Sci. Eng. 142 (1) (2019) http://dx.doi.org/10.1115/1.4045055.

[18] C. Casavola, A. Cazzato, V. Moramarco, C. Pappalettere, Orthotropic mechanical properties of fused deposition modelling parts described by classical laminate theory, Mater. Des. 90 (2016) 453–458, http://dx.doi.org/10.1016/j.matdes.2015.11.009.

[19] H. Gonabadi, Y. Chen, A. Yadav, S. Bull, Investigation of the effect of raster angle, build orientation, and infill density on the elastic response of 3D printed parts using finite element microstructural modeling and homogenization techniques, Int. J. Adv. Manuf. Technol. 118 (5) (2022) 1485–1510, http://dx.doi.org/10.1007/s00170-021-07940-4.

[20] A. Forés-Garriga, M.A. Pérez, G. Gómez-Gras, G Reyes-Pozo, Role of infill parameters on the mechanical performance and weight reduction of PEI Ultem processed by FFF, Mater. Des. 193 (2020) 108810, http://dx.doi.org/10.1016/j.matdes.2020.108810.

[21] Y. Qin, Q. Qi, P. Shi, P.J. Scott, X. Jiang, Status, issues, and future of computer-aided part orientation for additive manufacturing, Int. J. Adv. Manuf. Technol. 115 (5) (2021) 1295–1328, http://dx.doi.org/10.1007/s00170-021-06996-6.

[22] K. Thrimurthulu, P.M. Pandey, N. Venkata Reddy, Optimum part deposition orientation in fused deposition modeling, Int. J. Mach. Tools Manuf. 44 (6) (2004) 585–594, http://dx.doi.org/10.1016/j.ijmachtools.2003.12.004.

[23] P.K. Gurrala, S.P. Regalla, Optimization of support material and build time in fused deposition modeling (FDM), Appl. Mech. Mater. 110 (2012) 2245–2251, http://dx.doi.org/10.4028/www.scientific.net/AMM.110-116.2245.

[24] A. Dey, N. Yodo, A systematic survey of FDM process parameter optimization and their influence on part characteristics, J. Manuf. Mater. Process. 3 (3) (2019) http://dx.doi.org/10.3390/jmmp3030064.

[25] J.F.P. Lovo, C.A. Fortulan, M.M. da Silva, Optimal deposition orientation in fused deposition modeling for maximizing the strength of three-dimensional printed truss-like structures, Proc. Inst. Mech. Eng. B 233 (4) (2019) 1206–1215, http://dx.doi.org/10.1177/0954405418774603.

[26] M. Raju, M.K. Gupta, N. Bhanot, V.S. Sharma, A hybrid PSO–BFO evolutionary algorithm for optimization of fused deposition modelling process parameters, J. Intell. Manuf. 30 (7) (2019) 2743–2758, http://dx.doi.org/10.1007/s10845-018-1420-0.

[27] Y. Zhang, A. Bernard, An integrated decision-making model for multi-attributes decision-making (MADM) problems in additive manufacturing process planning, Rapid Prototyp. J. 20 (5) (2014) 377–389, http://dx.doi.org/10.1108/RPJ-01-2013-0009.

[28] Z. Chen, Y. Chen, Selection of build orientation with minimum tensile strain, Comput.-Aided Des. Appl. 7 (5) (2010) 639–647, https://www.tandfonline.com/doi/abs/10.3722/cadaps.2010.639-647.

[29] H. Shen, S. Guo, J. Fu, Z. Lin, Building orientation determination based on multi-objective optimization for additive manufacturing, 3D Print Addit. Manuf. 7 (4) (2020) 186–197, http://dx.doi.org/10.1089/3dp.2019.0106.

[30] J. Torres, J. Cotelo, J. Karl, A.P. Gordon, Mechanical property optimization of FDM PLA in shear with multiple objectives, JOM 67 (5) (2015) 1183–1193, http://dx.doi.org/10.1007/s11837-015-1367-y.

[31] O.A. Mohamed, S.H. Masood, J.L. Bhowmik, Mathematical modeling and FDM process parameters optimization using response surface methodology based on Q-optimal design, Appl. Math. Model. 40 (23) (2016) 10052–10073, http://dx.doi.org/10.1016/j.apm.2016.06.055.

[32] M.P. Zwier, W.W. Wits, Design for additive manufacturing: Automated build orientation selection and optimization, Procedia CIRP 55 (2016) 128–133, http://dx.doi.org/10.1016/j.procir.2016.08.040.

[33] C. Yu, L. Qie, S. Jing, Y. Yan, Personalized design of part orientation in additive manufacturing, Rapid Prototyp. J. 25 (10) (2019) 1647–1660, http://dx.doi.org/10.1108/RPJ-12-2018-0309.

[34] H.S. Byun, K.H. Lee, Determination of optimal build direction in rapid prototyping with variable slicing, Int. J. Adv. Manuf. Technol. 28 (3) (2005) 307, http://dx.doi.org/10.1007/s00170-004-2355-5.

[35] H.S. Byun, K.H. Lee, Determination of the optimal build direction for different rapid prototyping processes using multi-criterion decision making, Robot. Comput.-Integr. Manuf. 22 (1) (2006) 69–80, http://dx.doi.org/10.1016/j.rcim.2005.03.001.

[36] Y. Zhang, A. Bernard, R.K. Gupta, R. Harik, Feature based building orientation optimization for additive manufacturing, Rapid Prototyp. J. 22 (2) (2016) 358–376, http://dx.doi.org/10.1108/RPJ-03-2014-0037.

[37] E. Ulu, E. Korkmaz, K. Yay, O. Burak Ozdoganlar, L. Burak Kara, Enhancing the structural performance of additively manufactured objects through build orientation optimization, J. Mech. Des. 137 (11) (2015) http://dx.doi.org/10.1115/1.4030998.

[38] J. Liu, A.T. Gaynor, S. Chen, Z. Kang, K. Suresh, A. Takezawa, L. Li, J. Kato, J. Tang, C.C.L. Wang, L. Cheng, X. Liang, A.C. To, Current and future trends in topology optimization for additive manufacturing, Struct. Multidiscip. Optim. 57 (6) (2018) 2457–2483, http://dx.doi.org/10.1007/s00158-018-1994-3.

[39] M. Langelaar, Combined optimization of part topology, support structure layout and build orientation for additive manufacturing, Struct. Multidiscip. Optim. 57 (5) (2018) 1985–2004, http://dx.doi.org/10.1007/s00158-017-1877-z.

[40] D. Fischer, C. Eßbach, R. Schönherr, D. Dietrich, D. Nickel, Improving inner structure and properties of additive manufactured amorphous plastic parts: The effects of extrusion nozzle diameter and layer height, Addit. Manuf. 51 (2022) 102596, http://dx.doi.org/10.1016/j.addma.2022.102596.

[41] C.H.P. Nguyen, Y. Choi, Concurrent density distribution and build orientation optimization of additively manufactured functionally graded lattice structures, Comput. Aided Des. 127 (2020) 102884.

[42] J. Liu, H. Yu, Concurrent deposition path planning and structural topology optimization for additive manufacturing, Rapid Prototyp. J. 23 (5) (2017) 930–942, http://dx.doi.org/10.1108/RPJ-05-2016-0087.

[43] J. Liu, Y. Ma, A.J. Qureshi, R. Ahmad, Light-weight shape and topology optimization with hybrid deposition path planning for FDM parts, Int. J. Adv. Manuf. Technol. 97 (1) (2018) 1123–1135, http://dx.doi.org/10.1007/s00170-018-1955-4.

[44] Z. Shakeri, K. Benfriha, M. Shirinbayan, M. Ahmadifar, A. Tcharkhtchi, Mathematical modeling and optimization of fused filament fabrication (FFF) process parameters for shape deviation control of polyamide 6 using taguchi method, Polymers 13 (21) (2021) https://www.mdpi.com/2073-4360/13/21/3697.

[45] D. Jiang, R. Hoglund, D.E. Smith, Continuous fiber angle topology optimization for polymer composite deposition additive manufacturing applications, Fibers 7 (2) (2019) https://www.mdpi.com/2079-6439/7/2/14.

[46] M.P. Serdeczny, R. Comminal, D.B. Pedersen, J. Spangenberg, Experimental validation of a numerical model for the strand shape in material extrusion additive manufacturing, Addit. Manuf. 24 (2018) 145–153, http://dx.doi.org/10.1016/j.addma.2018.09.022.

[47] J. Baiges, C. Bayona, Refficientlib: An efficient load-rebalanced adaptive mesh refinement algorithm for high-performance computational physics meshes, SIAM J. Sci. Comput. 39 (2) (2017) C65–C95, http://dx.doi.org/10.1137/15M105330X.

[48] N. Dialami, M. Chiumenti, M. Cervera, R. Rossi, U. Chasco, M. Domingo, Numerical and experimental analysis of the structural performance of AM components built by Fused Filament Fabrication, Int. J. Mech. Mater. Des. (2020) http://dx.doi.org/10.1007/s10999-020-09524-8.

[49] I. Rivet, N. Dialami, M. Cervera, M. Chiumenti, G. Reyes, M.A. Pérez, Experimental, computational, and dimensional analysis of the mechanical performance of Fused Filament Fabrication parts, Polymers 13 (11) (2021) 1766.

[50] N. Dialami, I. Rivet, M. Cervera, M. Chiumenti, Computational characterization of polymeric materials 3D-printed via Fused Filament Fabrication, Mech. Adv. Mat. Struct. (2022).

[51] Y. Zhang, F. Li, D. Jia, Lattice impeller design and multi-scale stress-deformation analysis based on conventional cubic lattice, Mech. Adv. Mater. Struct. (2020) 1–17, http://dx.doi.org/10.1080/15376494.2020.1855681.

[52] Cura home page, 2022, https://ultimaker.com. (Accessed 25 January 2022).

[53] A.E. Kaufman, Voxels as a computational representation of geometry, in: SIGGRAPH, Vol. 94, 1994, p. 45.

[54] S. Ghadai, A. Jignasu, A. Krishnamurthy, Direct 3D printing of multi-level voxel models, Addit. Manuf. 40 (2021) 101929, http://dx.doi.org/10.1016/j.addma.2021.101929.

[55] G. Yu, J. Yang, On the robust shortest path problem, Comput. Oper. Res. 25 (6) (1998) 457–468, http://dx.doi.org/10.1016/S0305-0548(97)00085-3.

[56] J. Baiges, M. Chiumenti, C.A. Moreira, M. Cervera, R. Codina, An adaptive finite element strategy for the numerical simulation of additive manufacturing processes, Addit. Manuf. 37 (2021) 101650, http://dx.doi.org/10.1016/j.addma.2020.101650.

[57] S. Oller, E. Car, J. Lubliner, Definition of a general implicit orthotropic yield criterion, Comput. Methods Appl. Mech. Engrg. 192 (7) (2003) 895–912, http://dx.doi.org/10.1016/S0045-7825(02)00605-9.

[58] S. Kim, M. Cervera, J. Wu, M. Chiumenti, Strain localization of orthotropic elasto–plastic cohesive–frictional materials: Analytical results and numerical verification, Materials 14 (8) (2021) http://dx.doi.org/10.3390/ma14082040.

[59] M.A. Slawinski, Waves and Rays in Elastic Continua, World Scientific, 2010.
[60] V. Chandola, A. Banerjee, V. Kumar, Anomaly detection: A survey, ACM Comput. Surv. 41 (3) (2009) http://dx.doi.org/10.1145/1541880.1541882.
[61] H. P. Kriegel, P. Kröger, A. Zimek, Outlier detection techniques, in: Tutorial At the 13th Pacific-Asia Conference on Knowledge Discovery and Data Mining., 2009.
[62] M. Cervera, C. Agelet de Saracibar, M. Chiumenti, COMET: Coupled Mechanical and Thermal Analysis, Data Input Manual, Version 5.0, Technical Report IT-308, 2002, http://www.cimne.upc.es.
[63] GiD: The personal pre and post preprocessor, 2002, http://www.gidhome.com.
[64] R.M. Sakia, The box-cox transformation technique: A review, J. R. Stat. Soc. Ser. D (Stat.) 41 (2) (1992) 169–178, http://dx.doi.org/10.2307/2348250.